

**EFFECT OF CHANNEL ROUGHNESS ON MICRO DROPLET DISTRIBUTION IN
INTERNAL MINIMUM QUANTITY LUBRICATION**

A Thesis

by

MICHAEL THOMAS CRAIG

Submitted to the Graduate and Professional School of

Texas A&M University

in partial fulfillment of the requirements for the degree of

MASTER OF SCIENCE

Chair of Committee,
Committee Members,

Head of Department,

Wayne Nguyen Hung

Bruce Li-Jung Tai

Albert E. Patterson

Reza Langari

December 2022

Major Subject: Engineering Technology

Copyright 2022 Michael Thomas Craig

ABSTRACT

This research studied the effect of channel roughness on micro droplet diameter and distributions for two commercially available lubricants in internal minimum quantity lubrication (MQL). The effect of increased channel roughness in the nozzle of a MQL system was tested. Chemical etching was studied to control the roughness of external surfaces of tungsten carbide tools. Mixtures of oils and air were flown through internal channels with different simulated roughness: as fabricated, partially threaded, and fully threaded. Resultant micro-droplet sizes and counts were collected on a glass grid for evaluation. Droplet density was calculated to characterize the dispersion patterns of lubricant exiting the MQL system. The results were compared with outcomes of air flow simulations using a computational fluid dynamic approach. Nonparametric statistical analysis was conducted to further analyze the results of the MQL droplet characterization experiment. Chemical etching of tungsten carbide was done using a reagent of hydrogen peroxide and nitric acid. Hand agitation and a combination of hand agitation and ultrasonic pulsation were used to compare the rates of material removal. Scanning electron microscopy images were used to further analyze the surface structure of substrates before and after etching. For low viscous lubricant, the rough channel surface helped to break large droplets in the boundary layer into smaller droplets and reintroduce them into the main downstream flow. The opposite trend was found for lubricant with high viscosity, as increased lubricant wall adhesion inhibited the breakdown of droplets within the channel, leading to the dispersion of larger droplets. In chemical etching experiments, the synergy of hand and ultrasonic agitation successfully roughened a carbide surface within twelve minutes. Hand agitation alone was less successful, and resulted in smoother surface finishes. Scanning electron microscopy examination showed that the addition of ultrasonic pulsation enabled deep etching that removed all grinding marks on a WC-Co cutting tool surface.

DEDICATION

This thesis is dedicated to my father Thomas, mother Jeanette, sisters Nicole and Taylor, and brother Joseph. I am grateful for their support, encouragement, and motivation throughout my collegiate studies.

ACKNOWLEDGEMENTS

I give thanks to my committee chair Dr. Hung along with my committee members Dr. Tai and Dr. Patterson for their dedication to my studies and support of my research efforts. I also give thanks and appreciation to my fellow engineering technology and industrial distribution department members for making my time at Texas A&M University memorable. I am thankful for Amla Patel for her help in image capturing and processing, Jay Raval for his help with lubricant flow simulations, and Andrew Russel for his support on surface roughness measurements.

CONTRIBUTORS AND FUNDING SOURCES

This research was funded by the National Science Foundation under the GOALI Grant No. 1760985.

Kind support was provided by Ford Motor Company, Unist Inc., and Texas A&M University Microscopy and Imaging Center Core Facility RRID:SCR_022128.

NOMENCLATURE

ANOVA	Analysis of Variance
BUE	Built Up Edge
CFD	Computational Fluid Dynamics
CL	Coolube 2210Al
CT	Castrol Hyspray A1536
EDM	Electrical discharge machining
FT	Fully Threaded
HA	Hand agitation
HA + US	Hand agitation and ultrasonic pulsation
MQL	Minimum quantity lubrication
MIP	Male iron pipe
MOUDI	Micro Orifice Uniform Deposit Impactor
PT	Partially Threaded
T1	Trial 1
T2	Trial 2
3D	Three Dimensional
a	Droplet Radius
A	Area of droplet calculated by ImageJ
C	Constant for contact angle calculation
d	Airborne droplet diameter
K	Line tension
N	Airborne Droplet Diameter Constant
P	Projected droplet diameter
V	Volume of droplet
θ	Contact angle
γ_{LG}	Surface tension of liquid relative to gas
γ_{SG}	Surface tension of solid relative to gas

γ_{SL}

Surface tension of solid relative to liquid

TABLE OF CONTENTS

	Page
ABSTRACT.....	ii
DEDICATION.....	iii
ACKNOWLEDGEMENTS.....	iv
CONTRIBUTORS AND FUNDING SOURCES	v
NOMENCLATURE	vi
LIST OF FIGURES	x
LIST OF TABLES.....	xii
1. INTRODUCTION.....	1
1.1. Objective.....	2
1.2. Scope	2
2. LITERATURE REVIEW.....	3
2.1. Minimum Quantity Lubrication.....	3
2.1.1. Single vs. Dual Channel MQL Systems	3
2.1.2. External and Internal MQL.....	4
2.1.3. Effect of Internal Channel Geometry.....	6
2.1.4. Effect of Oil Type	8
2.1.5. Effect of MQL on Machining	10
2.2. Surface Modification	15
2.3. Ultrasonic Cleaning	17
2.4. Summary of Literature Review and Research Gap	18
3. EXPERIMENTS	19
3.1. MQL Droplet Characterization.....	19
3.1.1. Equipment.....	19
3.1.2. Materials	21
3.1.3. Methods.....	22

	Page
3.2. MQL Lubricant Flow Simulations	24
3.3. Chemical Etching of WC-CO	25
3.3.1. Equipment	25
3.3.2. Materials	26
3.3.3. Methods.....	27
3.4. Metrology	28
4. RESULTS AND DISCUSSION	31
4.1. MQL Droplet Characterization.....	31
4.2. MQL Mixture Flow Simulations	38
4.3. Nonparametric Statistical Analysis	43
4.4. Chemical Etching	47
4.5. Sensitivity Analysis	53
5. CONCLUSIONS	55
6. FUTURE WORK	57
REFERENCES	58
APPENDIX A. MQL DROPLET CHARACTERIZATION DATA	63
APPENDIX B. MICROSCOPE IMAGE PROCESSING.....	65
APPENDIX C. CHEMICAL ETCHING DATA	76
APPENDIX D. IMAGE FOCUS STACKING.....	83
APPENDIX E. PUBLICATION.....	85

LIST OF FIGURES

	Page
Figure 1. Single vs. Dual Channel MQL	4
Figure 2. Milling and External MQL Setup.....	5
Figure 3. Emulsion Fluid Delivery	12
Figure 4. Dual Helical Lubricant Delivery Channels on a Twist Drill.....	15
Figure 5. Micro droplet system. A: Air regulator, B: air flow meter, C: pressure gauge, D: MQL Unist Coolubricator, E: output nozzle, F: drop collection plate, and G: jack plate.....	19
Figure 6. Test Tip Assembly and Dimensions.....	20
Figure 7. Polar Coordinate Representation of Collection Zones. The Origin is at the Center of the Tip Projection at Location 5	21
Figure 8. Chemical Etching Setup. Where, A: Hot Plate, B: Glass Pan, C: 250 mL Beaker, D: Tool Hanger, E: Jack Plate, F: Ultrasonic Pulser, G: Chilled Bath	25
Figure 9. (A) Microscope Captured (B) Adobe Photoshopped (C) ImageJ Processed	28
Figure 10. Scanning Electron Microscope Vacuum Chamber.....	29
Figure 11. Resultant Microdroplet Images for Coolube and Castrol Lubricant at Location 7 (39.6 mm, 219°) and 690 kPa.....	31
Figure 12. Airborne Droplet Diameter Distribution for Different Lubricants.....	33
Figure 13. Effect of Radial Distance and Surface Roughness on Droplet Quality of Coolube (CL) and Castrol (CT). S: Smooth, PT: Partially Threaded, FT: Fully Threaded.....	36
Figure 14. Lubricant Flow Velocity Vectors	41

	Page
Figure 15. Residuals Compared to Normal Probability Plot	43
Figure 16. Main Effect of Lubricant Type, Radial Distance, and Channel Roughness on Airborne Droplet Size	44
Figure 17. Interaction Between Input Parameters for MQL Droplet Characterization Tests ..	45
Figure 18. Change in surface roughness of WC-Co with etching time.	48
Figure 19. 1000x Image of Etched (A) 12 Minute HA and (B) 12 Minute HA + US Inserts .	49
Figure 20. SEM Images for 12 Minute HA and HA + US Trials	50
Figure 21. Optical Images for 12 Minute HA and HA + US Trials.....	52

LIST OF TABLES

	Page
Table 1. Resultant Average Droplet Diameters (μm)	6
Table 2. Surface Roughness and Flank Wear vs. Machining Time.....	11
Table 3. Air and Oil Flow Rate Effect on Flank Wear and Tool Temperature.	13
Table 4. Effect of Air Pressure and Channel Type on Surface Roughness and Tool Wear. ...	13
Table 5. Lubricant Type and Feed Rate Effect on Surface Roughness.	14
Table 6. Tested Lubricants and Properties.....	22
Table 7. MQL Droplet Collection Parameters	23
Table 8. MQL Droplet Characterization Experimental Design	24
Table 9. MQL Simulation Boundary Conditions.....	25
Table 10. Statistical Analysis of Airborne Droplet Diameters.	34
Table 11. Kruskal-Wallis Test Results	44
Table 12. Surface Roughness Before and After Etching.	47
Table 13. Sensitivity Analysis	54

1. INTRODUCTION*

Machining operations use lubrication to maintain tool integrity, reduce tool wear rate and heat of machining, reduce friction for better chip formation, increase tool life and decrease power consumption, and produce smoother workpiece surface finishes [1]. It is very difficult to direct coolant to the cutting edge of a drill bit in a deep drilling operation using traditional external lubrication techniques. Lack of adequate lubrication leads to large frictional forces that cause accelerated tool wear and less precision in machining operations [1]. Traditional methods, such as flood cooling, spray large amounts of lubrication across the cutting surface. Most of the coolant is not needed because it does not reach the tool chip interface. A disadvantage of flood lubrication is the need for a secondary system to capture, filter, and dispose lubricant after machining. An advantage of MQL is that it is a much cleaner system than flood cooling and there is no need for fluid recycling.

MQL delivers micro droplets of lubricant directly to the cutting zone using external or internal delivery methods. External MQL is typically used in milling, turning, sawing, and grinding operations. Internal MQL is more common in milling and drilling, and lubricant delivery channels output cutting fluid near the tool edge. In drilling operations, internal channels aim fluid directly to the cutting edge of the drill bit. MQL decreases operating costs, as less lubrication is required for machining.

Previous studies involving MQL have largely focused on the effects that channel geometry and mist parameters have on tool life and workpiece finish using external or internal delivery methods [1-28]. Studies were found for internal MQL that described the resulting droplets and droplet distribution due to different shape and size of coolant channels. Limited experimental work was performed to show the effect of channel surface roughness on droplet size, its distributions and machining operations. A more comprehensive study on the impact of channel surface roughness, therefore, was sought.

*Reprinted with permission from “Effect of Channel Roughness on Micro-Droplet Distribution in Internal Minimum Quantity Lubrication” Craig M., Raval J., Tai B., Patterson A., and Hung W., Dynamics, vol. 2, no. 4, pp. 336–355, by the authors 2022.

1.1. Objective

This research (i) characterizes the effect of channel surface roughness on MQL droplet size and (ii) studies methods of modifying the surface of WC-Co drill channels to improve high aspect ratio drilling performance.

1.2. Scope

The MQL experiment compared the droplet size and dispersion with simulated smooth, medium roughness, and very rough surfaces in the outlet of the MQL system nozzle. The study used Coolube and Castrol lubricants for comparison. Average droplet size was calculated for both lubricant types flowing through each channel. Droplets were captured from a grid system used to characterize the effect of radial distance on droplet dispersion. Computer simulated flow analysis of experimental results were used for comparison. Methods to modify the surface of WC-Co drill channels were explored. A chemical etching process was tested to control the surface roughness of WC-Co substrates. Two types of agitation were tested to compare the resultant surface roughness, and three etching times were used.

2. LITERATURE REVIEW*

2.1. Minimum Quantity Lubrication

Efforts to reduce consumption of lubricants have been driven by economic and environmental concerns. Lubrication techniques are deployed to remove heat, control tool wear, and aid in chip removal during machining operations. At low cutting speeds flood coolant achieves all three of these objectives, but as the cutting speed increases coolant cannot reach the cutting zone and this method becomes ineffective [1]. MQL has emerged as a way to reduce the amount of coolant used and increase lubrication performance at high machining speeds. It uses a pressurized mix of air and lubricant sprayed directly onto the cutting zone. MQL can be administered externally using nozzles positioned above the workpiece, or internally by through tool delivery. In machining applications, MQL has become increasingly popular as it decreases manufacturing costs, reduces negative environmental impacts, simplifies cleaning processes, and increases tool life [1-2]. Smaller MQL droplets provide better lubrication which decreases tool wear and leads to smoother surfaces on the machined workpiece [3].

2.1.1. Single vs. Dual Channel MQL Systems

There are two main system designs used in internal MQL, single and dual channel (Figure 1). In single channel systems, the lubricant and pressurized air are mixed externally and routed through the system spindle [2]. External mixing is done using a metering pump or pressurized tank [4]. The metering pump method utilizes a positive displacement micro pneumatic pump to connect the lubricant flow with an air blast nozzle. Oil volume is controlled by the pump speed. The pressurized tank method uses a pressurized lubricant tank and venturi nozzle to mix the aerosol solution. The oil quantity delivered is adjusted by the tank pressure. In single channel systems, the rate of oil delivery is dependent on air flow rate [4]. In a dual channel setup, air and lubricant are routed through the system in separate channels, and the two streams are mixed together near the tool point, or system outlet [2]. The rate of oil delivery is controlled using a positive displacement pump with a built in speed controller, or a pressurized oil tank with a metering valve [4]. In dual channel systems, the oil delivery rate is

*Reprinted with permission from “Effect of Channel Roughness on Micro-Droplet Distribution in Internal Minimum Quantity Lubrication” Craig M., Raval J., Tai B., Patterson A., and Hung W., Dynamics, vol. 2, no. 4, pp. 336–355, by the authors 2022.

independent of the air flow rate. Both systems have advantages and disadvantages. Single channel setups are much less expensive than dual, and they are popular in sawing operations as dimensional tolerances are more relaxed and the surface roughness is not an important control metric. The drawbacks of single channel systems include large lubricant droplets due to the longer travel of the aerosol mixture, and instability of mist quality due to the effect of inertial and centrifugal force when delivered to the tool tip [2]. Dual channel setups offer a more robust lubricant delivery. They result in less dispersion of the aerosol mixture and deliver finer and more uniform mist than single channel systems. The biggest disadvantage of dual channel systems is the added cost when compared to single channel.

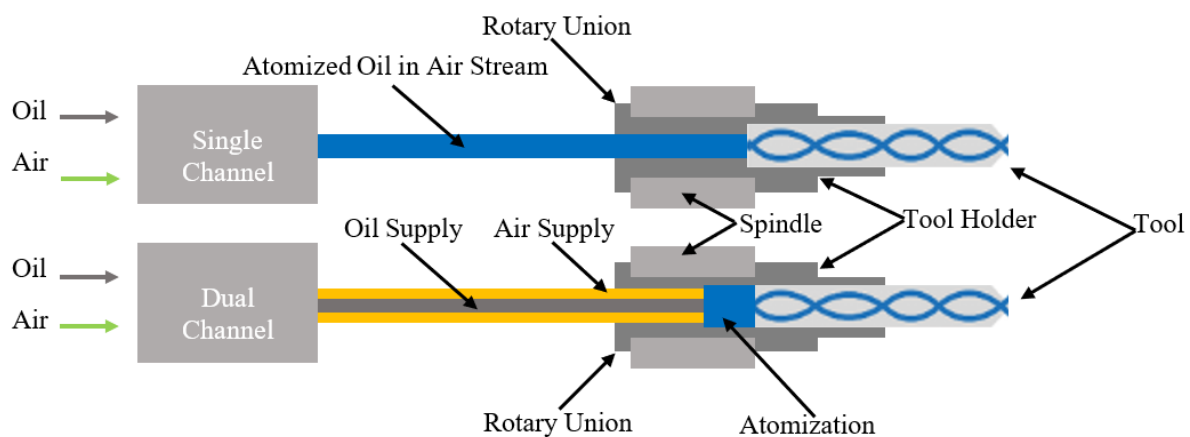


Figure 1. Single vs. Dual Channel MQL

2.1.2. External and Internal MQL

Race et al. [5] compared external MQL and flood coolant in face milling operations using SA516 grade 70 steel plates and vegetable-based oils. The plates were 250 x 250 x 70 mm in size. A three axis Hartford LG500 vertical mill was used with a 40 mm diameter Coro-mill 300 face mill paired with R300-1240E-PL grade 4240 carbide inserts coated with Ti(C, N)+Al₂O₃+TiN (Figure. 2). A SKF MQL system was used to deliver mist at 45 mL/hr. This research concluded that MQL reduced tool flank wear and surface roughness of the machined part. The effect of each coolant type on the machining energy footprint was also studied. MQL resulted in a 1.5 kW reduction in peak machine power when compared to flood coolant. This showed that MQL was more economic than flood coolant not only because the reduction in lubricant used, but a reduction in energy consumption as well.

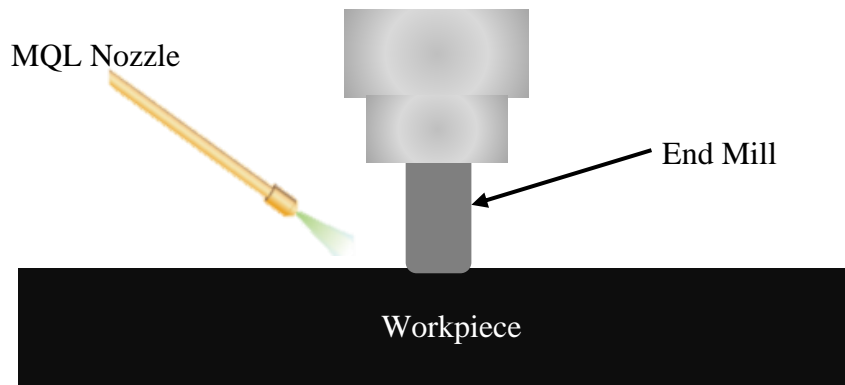


Figure 2. Milling and External MQL Setup

Hwang et al. [6] turned AISI 1045 with external MQL and flood lubricant methods. A Hwacheon Hi-ECO 10 turning center paired with a Vogel Vario UFV 10-001 MQL system was used to conduct the experiment. Empirical equations were derived to verify the results of the machining operations. The study showed that lower surface roughness was achieved at a higher feed rate using MQL as compared to wet lubrication (0.02 mm/rev and 0.01 mm/rev feed rates respectively). If cutting force and surface roughness are considered, MQL is more advantageous than wet lubrication. Both methods resulted in similar cutting forces, but MQL achieved better surface roughness (approximately 30% less rough when compared to wet lubrication).

Li et al. [7] compared dry machining and external MQL using an experimental approach in grinding operations on a SK3 with HRC18 workpiece. The desktop grinder used was equipped with a high speed spindle and three axis machining table. A 600 μm diameter #200 grinding tool was chosen for the experiment. Vegetable based oil was run through the MQL system at 1.88 mL/hr and 0.5 MPa pressure. The external MQL delivery setup was similar to that shown in Figure. 1, using a micro-grinder in place of an end mill. This work showed that surface roughness did not change as a function of feed rate or cutting speed using MQL. Dry cutting led to an overall rougher surface finish. It was observed that the use of MQL increased grinding wheel life 7x versus dry grinding operations.

Khan et al. [3] used an experimental based approach to study the micro droplet distributions created in through-tool internal MQL. 3D printed ABS plastic adapters were used to simulate polished (3.2 μm Ra) vs. rough (16.8 μm Ra) surface finishes. These adapters were connected to the outlet nozzle of a Unist Coolubricator system. Coolube 2210EP lubricant was used to create micro droplets, and an Arrow B754FM air regulator controlled the inlet air pressure. Three tests were conducted using 275 kPa (40 psi), 415 kPa (60 psi), and 550 kPa

(80 psi) inlet air pressures. Table 1, interpreted from the results of this experiment, showed that as the surface roughness increased in the nozzle adapters, the resultant average droplet diameter decreased. The air pressure also affected the droplet size. At lower pressures, larger droplets were formed.

Table 1. Resultant Average Droplet Diameters (μm). Adapted From [3]

Pressure (kPa)	Rough Adapter (16.2 μm)	Polished Adapter (3.2 μm)
275	9.2	11.42
415	7.25	9.31
550	4.69	7.6

Tasdelen et al. [8] studied internal MQL versus emulsion lubrication in drilling operations using through tool delivery. The tests were conducted using a Modig MD 7200 drilling center at 15000 rpm paired with a Lubri Lean-Vario Super MQL system. MQL led to less tool wear and smoother surface finish in the drilled holes. The study also tested continuous MQL delivery compared to interrupted flow (23 mL/hr, 15 mL/hr, and 5 mL/hr fluid delivery). In continuous, the WC-Co tool inserts showed less wear after drilling operations. The best hardened-steel workpiece surface finish result came from 15 mL/hr MQL delivery.

Maruda et al. [9-10] studied external MQL emulsion mist generation. Maruda's work characterized the effect of air flow, emulsion flow, and nozzle to work-piece distance on the size and count of micro-droplets. In this study, water soluble OPORTET RG-2 emulsion, commonly used in milling, turning, and threading operations, was tested at a 2% concentration in water. The results showed that air flow rate and the distance between the nozzle and cutting zone had the most significant impact on droplet diameter. An increase in either caused the droplet size to decrease and count to increase. Changes in emulsion flow had less impact on the droplet distributions.

2.1.3. Effect of Internal Channel Geometry

Past studies have been used to characterize the effects that channel shape and size have on droplet distributions in internal MQL [11-13]. Raval et al. [11-12] used two experiments to study straight vs. helical channels and circular vs. triangular channels at different helical angles. The first experiment utilized a non-coherent white light tomography approach

paired with a high speed camera to capture the lubricant stream exiting internal channels of a stereolithography additive manufactured drill bit. A Unist Coolubricator dual channel MQL system was used to generate microdroplets using Castrol Hyspray Al536 lubricant. Both the straight and helical channels were located 2.5 mm from the drill bit axis, and had circular cross sections 2 mm in diameter. The channel length was held constant at 70 mm, and the helical channels had a 30° helix angle. The results showed that straight channels experienced annular flow due to high velocity in the axial direction. This led to higher momentum in the axial direction than the radial momentum generated by centrifugal force from drill rotation, which caused lubricant wall adhesion [11]. In the helical channels, no annular flow was recorded. These channels generated secondary vortices within that disrupted the annular distribution.

In Raval's second experiment [12] the cross section geometry and helical angle of internal channels was studied using stereolithography 3D printed drill bits. Three different channel shapes were tested; circular, triangular, and reversed triangular (triangles rotated 180°). Each channel was tested using 0°, 30°, and 45° helix angles. The circular channels used had 1.6 mm diameters, and the triangular channels were equilateral with 2.15 mm side lengths. MQL mist was generated using a Unist Coolubricator with Coolube 2210 lubricant at 40 mL/hr, a rotary union, and an atomizing chamber. A high speed camera was used to capture the lubricant flow leaving the drill bit. The channels were centered 2.5 mm from the drill bit axis. Because of this small distance, centrifugal force due to drill bit rotation was negligible. The 0° circular channel showed high mist concentration at the outer edges, and low concentration in the center. This created annular flow causing air to travel through the center of the channel and lubricant along the outer walls. The 30° and 45° circular helix channels created an elliptical shape at the chisel edge. Both resulted in low mist concentration zones away from the chisel edge. This created a wider high mist concentration near the chisel edge, and narrower concentration zone near the drill origin. The 0° triangle channel showed high mist concentrations at the vertices, and low concentration in the center of the channel. In the 30° helical triangular channel, the low mist concentration zone shifted downward. In the 45° helical triangular channel the low concentration zone shifted upward. The reversed triangle channels mirrored the results of the triangular channels, as the mist distributions shifted 180°. This showed that droplet distribution is dependent on the channel orientation. With the changes in mist characteristics for each channel tested, this experiment showed that channel shape, helix angle, and orientation affect the mist distribution.

Kao et al. [13] used an experimental approach with high speed image capturing paired with CFD models to characterize the resultant mist patterns in circular and triangular channels of varying size using internal MQL drill bits. Stereolithography additive manufacturing was used to make drill bits with four different channel geometries; Large equilateral triangle with side lengths of 2.15 mm, large circle with 1.6 mm diameter, small equilateral triangle with 1.35 mm side length, and small circle with 1 mm diameter. The MQL mist was generated using a Unist Coolubricator at 70 psi air pressure, 45 mL/hr fluid delivery, and a drill bit rotational speed of 1000 ± 30 rpm. The results of this study showed that mist structures varied significantly with changing channel geometries. Larger channels showed higher air speeds overall, and the circular channels resulted in higher air speeds than triangular. Smaller channels also experienced increased droplet coalescence, which caused mist to transition into lubricant flow. In the circular channels, flow structure tended to be concentrated toward the center of the drill bit. In triangular channels, the flow became concentrated in the vertices. This was consistent with the results seen by Raval. CFD models confirmed these experimental results.

2.1.4. Effect of Oil Type

Many researchers have worked to classify the effects that oil type has on machinability in MQL systems [14-16]. Yildirim et al. [14] used Waspaloy nickel-based super alloy in milling operations to test the effects of four different oil types on machinability. These four oils included mineral, synthetic, mineral-synthetic, and vegetable based. A delta Seiki CNC-1050 vertical mill was used with a R300-025A20-10M tool holder and K13A-quality uncoated cementite carbide tips to conduct milling operations in the experiment. A cutting speed of 45 m/min, feed rate of 0.01 mm/rev, and cut depth of 0.5 mm was used. Wear conditions of the cutting tools were examined, and regular flank and notching was observed to determine the effect that each oil type had on machinability. The MQL mist was generated using a Vario model from SKF set to 8 bar constant pressure. The results of this experiment showed that vegetable oil achieved the longest tool life, and tool life decreased with synthetic, mineral, and synthetic-mineral based oils respectively. Vegetable oil performed best because its surface tension and viscosity allowed better penetration into the cutting zone. This allowed better lubrication between the tool and workpiece. The vegetable based oils formed a thin and lasting layer of lubricant in the cutting zone. When compared to the other three oil

types, this led to a reduction in cutting force and friction which promoted longer tool life and better machinability.

Tai et al. [15] compared nine cutting fluids (biodegraded esters, renewable acid esters, naturally derived synthetic, vegetable based, vegetable based + sulfurized extreme pressure (EP), natural fatty oils, and synthetic ester listed in order of increasing viscosity) in terms of physical properties, bench tests, and machining tests to determine the effects that various lubricants have on MQL operations. The physical properties studied included density, viscosity, flash point, and thermal conductivity. In machining operations, the same amount of heat was generated for both MQL and flood lubricant methods, but there was less fluid in MQL to dissipate the heat. Because of this, thermal properties of lubricants determined the ability to remove heat. Thermal conductivity was measured at 25°C, 50°C, 75°C, and 90°C using a KO₂ pro thermal property analyzer. It was determined that water based traditional machining lubricants had higher thermal conductivity than common MQL fluids. This indicates that MQL fluids have lower heat removal capabilities. When compared to water based lubricants, MQL fluids had consistent thermal conductivity across all four temperatures, showing that thermal conductivity is independent of temperature. As viscosity increased, thermal conductivity also increased in MQL fluids.

The bench tests conducted by those authors included wettability, lubricity, and extreme pressure properties. Wettability is the contact angle between the lubricant droplets and workpiece surface in thermal equilibrium with each other and the gas phase. Lower contact angles decrease a droplet's ability to roll, increasing wettability. The contact angle of each lubricant on 6061 aluminum and WC was measured using a sessile droplet test with a DAS 10 drop measurement system made by KRUSS. The results showed that MQL lubricant had lower contact angles and better wettability when compared to water based lubricants. A Microtap USA tapping torque machine was used to study lubricity of each lubricant using a pre-drilled aluminum 6061 workpiece tapped with a M8 tool steel tap at 1200 rpm. The results showed that water based lubricants had poorer lubricity as they resulted in higher tapping torques when compared to MQL fluids. Extreme pressure tests evaluate the lubricant performance under intense machining conditions. A Falex pin-and-vee-block was used to test each lubricant. Better extreme pressure properties were indicated by a higher load needed to shear the pin. On average, water based and MQL lubricants performed very similarly. A MOUDI from MSP corporation was used to study the microdroplet distribution created for each

lubricant. The MOUDI system was run at 30 L/min for 30 minutes. The MQL lubricants resulted in mist concentrations from 8.84 to 11.8 mg/m³ and average droplet diameters from 2.9 μm to 4.07 μm. The overall trend showed that decreasing viscosity created higher mist concentrations and larger average droplet diameters.

Those authors drilled and reamed spool bores in cast 393 aluminum to characterize the effect that each lubricant had on power consumption and hole quality. An Enshu JE50S CNC was used with a spindle speed of 12000 rpm. A large majority of the tested MQL fluids resulted in higher power consumption than the experimental standard MQL lubricant. A Taylor Hobson Talysurf profilometer was used to measure the surface roughness of the reamed holes, and diameters were measured with an air column gauge. The MQL fluids with lower viscosities showed finer surface finishes and more accurate hole dimensions. The main correlations were:

1. Low viscosity resulted in high wettability, high mist concentration, and larger droplet diameters.
2. Large mist diameters correlated with less energy consumption, smoother surface finish, and more accurate machined dimensions.
3. Higher wettability led to better dimensional accuracy.

The study concluded that low viscosity, large mist droplet diameter, and high wettability enhanced machinability.

2.1.5. Effect of MQL on Machining

Said et al. [17] reviewed how MQL affects turning, milling, drilling, and grinding. Comparisons were drawn between dry machining, flood lubricant, and MQL. The results are detailed below:

1. In turning operations, experimental studies showed that MQL improved tool life by approximately 25% when compared to dry machining. MQL reduced cutting power, improved surface roughness, reduced cutting force, and increased chip formation when compared to flood coolant, while using lesser lubricant quantities [18-19]. Dhar et al. [20] deployed a plain turning process on 125 mm diameter, 760 mm length AISI-4340 steel rod using a 15 hp Lehmann Machine Company lathe. The

cutting force, cutting temperature, tool wear, surface roughness, and dimensional accuracy was measured to compare dry, wet, and MQL lubrication techniques. When compared to dry and wet machining, MQL showed a decreased temperature at the interface between the cutting tool and workpiece. The lesser quantity of lubrication allowed the MQL aerosol mixture to be elastically drawn across the cutting zone by capillary effect, which created a more effective cooling ability. The high pressure flow of MQL allowed for removal of small chips which helped the lubricant reach the tool-chip contact zone. Using MQL, tool hardness was retained due to lesser abrasive tool wear. MQL reduced the rate of growth of tool flank wear because of a reduction in flank wear temperature. These effects led to an increased tool life when compared to wet and dry machining. The part's surface roughness was affected by residual feed marks left by the tool tip, irregular deformation of the tool cutting edge due to fracturing and wear, machine vibration, and BUE. Because MQL reduced tool wear, surface roughness grew more slowly using MQL compared to dry machining. After 45 minutes of machining, MQL resulted in a surface roughness of 4.25 μm Ra compared to 6.25 μm Ra in wet machining (Table. 2). MQL also improved surface finish by reduced abrasion, tool chipping, and BUE formation. The maximum principle flank wear for MQL inserts was ~ 225 μm less than that of dry machining.

Table 2. Surface Roughness and Flank Wear vs. Machining Time. Adapted From [20]

Machining Time (mins)	Surface Roughness Ra (μm)			Average Principle Flank Wear (μm)		
	MQL	Dry	Wet	MQL	Dry	Wet
15	3.25	3.75	4.00	140	150	125
30	3.50	4.40	4.75	225	280	275
45	4.25	5.00	6.25	350	475	480

Chetan et al. [21] characterized the wear behavior of PVD TiN coated carbide turning inserts when machining Nimonic 90 and Ti6Al4V. A MQL emulsion mixture (10:1 ratio of water and sunflower oil) was used in comparison with dry machining. Figure 3 shows where the lubricant was delivered in reference to the tool-chip interface. The results showed that applying the mixture to Ti6Al4V allowed ample wetting, decreasing the intensity of flank wear at high cutting speeds. The lubricant also better penetrated the surface of the Ti6Al4V workpiece, reducing flank wear when compared to Nimonic 90.

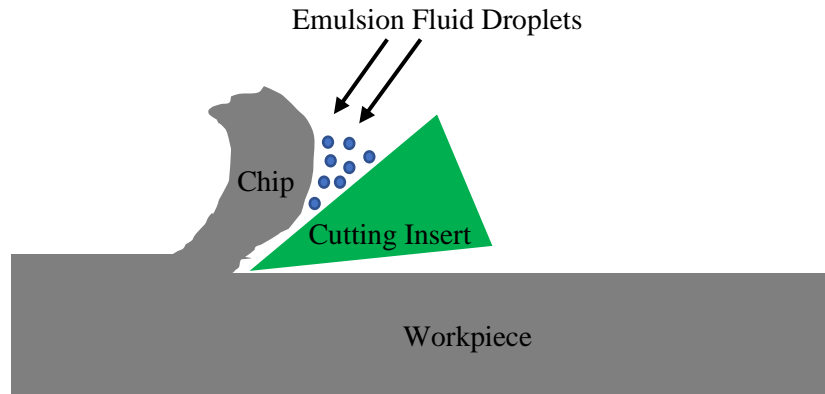


Figure 3. Emulsion Fluid Delivery

2. In milling operations, dry machining was used due to the increase in crack propagation in the tool because of temperature fluctuation. An issue with this was seen in difficult to machine materials, where the temperature in the cutting zone became very high. This led to poor machinability and tool wear, and because of this MQL was introduced into milling operations. MQL was more effective than flood cooling at low cutting speeds for milling, as it led to lower cutting force due to a reduction in adhesion and frictional forces (~ 5 N reduction) [22]. Iskandar et al. [23] studied the effect of air and oil flow rate and nozzle distance from the cutting zone on MQL flow characteristics. These effects were then compared to flood coolant in milling operations to study the resulting cutting force, temperature, tool wear, and dimensional accuracy. Particle image velocimetry and phase doppler anemometry visualization methods were used to define MQL flow. Air flow rates of 20, 25, 28, 31 L/min and oil flow rates of 10, 17.5, 24 mL/min were tested. The study showed that as air and oil flow rate increased, flow velocity increased. As the distance from the nozzle to the cutting zone increased the flow velocity decreased, and the droplet size and count increased. Optimal MQL spray was obtained by combining the maximum air flow rate (31 L/min) and minimum oil flow rate (10 mL/min), generating a large number of small droplets. In milling operations, various combinations of MQL air and oil flow rates showed similar tool temperatures (only 7% variation). The optimal MQL spray generated temperatures on the high end of the data set. Feed force was the same for MQL and flood coolant. Tool wear was 20-30% less using MQL when compared to flood coolant (Table. 3). The optimal MQL spray generated the lowest tool wear (17% less than other MQL combinations). MQL also held better dimensional accuracy than flood coolant, with the optimal spray satisfying the tool requirement of ± 10 μm .

Table 3. Air and Oil Flow Rate Effect on Flank Wear and Tool Temperature.

Adapted From [23]

Air Flow Rate (L/min)	Oil Flow Rate (mL/min)	Flank Wear (μm) at 450 mm Cutting Length	Tool Temperature ($^{\circ}\text{C}$) at 450 mm Cutting Length
N/A	Flood Coolant	30	N/A
31	24	28	300
20	24	25	270
31	10	22	280

In micromilling, MQL was studied to compare the effect of droplet size and air speed on surface roughness and tool wear [3]. High pressure MQL (550 kPa) increased air speed, and when paired with a rough lubricant delivery channel (16.8 μm Sa) a $\text{\O}5$ μm average droplet size was achieved. Low pressure MQL (275 kPa) decreased air speed, and when paired with a smooth lubricant delivery channel resulted in a $\text{\O}9$ μm average droplet size. At a milling distance of 20 mm the high pressure-rough channel test resulted in approximately 1.5 μm Sa surface roughness and 10 μm tool wear. At the same milling distance the low pressure-smooth channel resulted in approximately 2.75 μm Sa surface roughness and 25 μm tool wear (Table. 4).

Table 4. Effect of Air Pressure and Channel Type on Surface Roughness and Tool Wear. Adapted From [3]

Air Pressure (kPa)	Channel Type	Surface Roughness Ra (μm) at 20 mm Milling Distance	Tool Wear (μm) at 20 mm Milling Distance
275	Rough	2.45	30
275	Smooth	2.75	25
550	Rough	1.50	10
550	Smooth	2.15	22

3. In drilling operations, MQL delivered better machining performance when compared to dry machining. Rahim et al. [24] compared MQL and dry machining using drilling operations on the titanium alloy TI-6Al-4V. This study showed that dry machining resulted in a much shorter tool life when compared to MQL (0.2 mm tool wear at cutting lengths of 100 mm and 450 mm respectively) due to chipping, high temperatures, and increased frictional force. Drilling experiments on a AA1050 aluminum workpiece using a K10 drill bit were conducted by Davim et al. [25] to compare flood cooling and MQL. The results showed that the surface finish, cutting power, and cutting force required for MQL and flood coolant were very similar.

Surface roughness measurements were approximately 3.5 μm , 2.25 μm , and 2.0 μm Ra for dry, flood coolant, and MQL respectively using .15 mm/rev feed rate and 75 m/min cutting speed (Table. 5). The cutting power and specific cutting force was approximately 500 W and 2500 MPa across all three methods. In these experiments MQL was achieved using fluid deliveries in order of mL/hr compared to L/hr for flood coolant.

Table 5. Lubricant Type and Feed Rate Effect on Surface Roughness. Adapted From [24]

Lubricant Type	Feed Rate (mm/rev)	Surface Roughness Ra (μm) at 75 m/min Cutting Speed
Dry	0.15	3.50
	0.25	5.00
MQL (250 mL/hr)	0.15	2.25
	0.25	2.30
Flood Coolant (120 L/hr)	0.15	2.00
	0.25	2.05

Patil et al. [26] compared MQL to dry and flood coolant in through tool delivery drilling. This two-level factorial experiment was aimed at studying the effect of air pressure (413, 620 kPa) and MQL oil quantity (40, 60 mL/hr) on machinability. Flood coolant was delivered at 340 and 5678 L/hr using pressures of 76 and 83 kPa. A380 aluminum plates were drilled using $\varnothing 8$ mm drills, at 250 m/min cutting speed, 9950 rpm spindle speed, 0.20 mm/flute chip load, and 3980 mm/min federate. Hole oversize (μm) and cylindricity (μm) was measured to compare the drilling results of each lubricant. Oil quantity did not affect drilling quality. Economically, either MQL lubricant delivered in small quantities would be more advantageous than flood coolant.

The higher viscosity MQL lubricant (28 mm^2/s compared to 14.5 mm^2/s) provided the lowest hole oversize of 5.0 μm . Flood coolant resulted in the best hole shape, having the lowest cylindricity of 6.1 μm . This was possibly a result of low heat under flood cooling reducing thermal distortion. The cutting flute profiles were studied after drilling for both MQL fluids. The lower viscous lubricant, which formed a smaller contact angle on aluminum, provided smaller airborne droplets and better wetting and lubrication. This decreased BUE formation, which in turn decreased the surface roughness of drilled holes. This work showed that in internal MQL drilling, smaller microdroplets increased wetting capability, allowing the lubricant to further penetrate the tool-chip interface and cool the chip and tool more effectively.

2.2. Surface Modification

Many manufacturing processes can be used to control the surface of a workpiece: EDM, grinding, polishing, lapping, and sand blasting. Applying any of these processes to internal lubricant delivery channels of a drill is a challenge. Many drills incorporate helical channels for lubricant delivery (Figure 4). Because of small geometry, the methods listed above cannot be applied as it would be very difficult to access the internal surface of the channels using traditional contact methods. Liquid flow or slurry based methods can be used for internal surface modification.

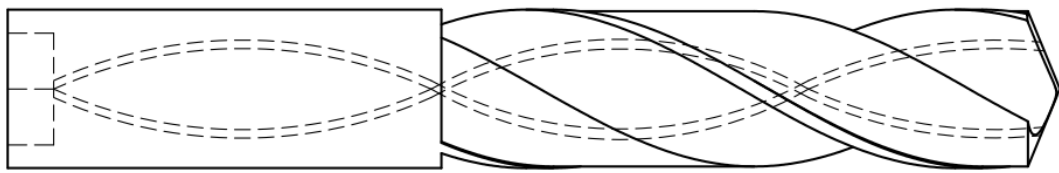


Figure 4. Dual Helical Lubricant Delivery Channels on a Twist Drill

An applicable method for roughening the surface of metallic workpieces is chemical etching. The process can be accelerated by raising the temperature or adding ultrasonic agitation. Etching is most commonly applied to external surfaces to increase the surface roughness and/or improve adhesion properties for coatings.

Chemical etching of WC-Co has been conducted using a two stage etching process [29-32]. The first stage used Murakami Solution ($K_3[Fe(CN)_6]$) or similar solutions to break down WC. The submersion time for this step varied from 5-80 minutes. The second step in this process was etching of the Co binder. This was done using multiple different acids.

Haubner et al. [29] conducted trials on hard metal inserts (94% WC, 5.5% Co, 0.5% (Ta, Nb)C) using a Murakami solution (10g $K_3[Fe(CN)_6]$, 10g KOH, 100ml H_2O) pretreatment paired with a Caro's acid etching process (5% H_2SO_4 , 35% H_2O_2). This study was performed to improve adhesion of diamond coatings on metal workpieces by pretreating the surface. Before etching, the substrates were cleaned using water. Trials were conducted using Murakami etching times of 0, 5, and 80 mins with and without a 10 second post-etching process using Caro's acid. SEM images were captured to study the surface finish after each etching trial. The author observed that the Murakami solution dissolved WC particles after 5 minutes of submersion, leaving the Co binder. Past 5 minutes, very little change was observed in the

surface structure. In trials that began with a Murakami solution etch, the 10 second etching process with Caro's acid partially dissolved the Co binder, leaving a textured surface finish. Microprobe measurements were used to show that Caro's acid rapidly removed the Co binder. When Murakami etching did not precede the Caro's acid etch, the process had little effect on the substrate. The Co binder was still present in the surface of the workpiece after the 10 second Caro's acid etching.

Chakravarthy et al. [30] performed a similar experiment to Haubner in using a two-step Murakami solution and Caro's acid etching process to study the effect on a WC-Co (8% Co) substrate. This study was conducted to increase the surface roughness of WC-Co tools such that adhesion of diamond deposition particles could be improved. Coatings were studied to improve tools used for machining hypereutectic aluminum-silicone alloys commonly used in the automotive industry. The research team used an ultrasonicator to agitate the substrate in Murakami solution for 30 minutes, followed by a 15 second Caro's acid etch. After etching, the substrates were cleaned with ethanol such that they could be seeded with diamond nanoparticles. SEM images showed that the as purchased WC-Co substrates had an average grain size of about 1 μm . It was shown that the Murakami solution roughened the substrate surface by removing WC particles. Caro's acid etching then caused oxidation of the Co binder to a soluble Co^{2+} compound. This caused a reduction in the concentration of Co on the substrate surface.

Sha et al. [31] studied the effects of etching on WC-Co (15% Co) using a two-step process of Murakami solution combined with a $\text{HNO}_3:\text{HCl}$ (1:1 ratio) etching solvent. This study was used to improve adhesion of diamond coatings on the surface of WC-Co substrates. The workpieces used in this study were 9 x 5.5 x 3 mm grounded pieces. The initial grinding process yielded a substrate surface roughness of 0.2 $\mu\text{m Ra}$. The process utilized a 1-3 minute Murakami reagent etch followed by a 10-40 minute $\text{HNO}_3:\text{HCl}$ etch. After etching the parts were cleaned in an ultrasonically pulsed acetone bath and weighed to determine the weight loss during etching. The overall results of this experiment were an increase in weight loss and decrease in hardness as etching time increased. The researcher observed that as the etching time in the second step increased the weight loss increased significantly up to 30 minutes. Longer etching periods resulted in only slight increases in substrate weight loss. After the two step etching process the resultant surface roughness was increased to 1.0 $\mu\text{m Ra}$. The Co binder content decreased from the original 15% to a range of 0.84-6.04%. An

overall etching depth of 5-10 μm was achieved. The authors concluded that the Murakami solution first removed WC grains, allowing the acid to deplete the Co binder.

Jung et al. [32] performed chemical etching on WC-Co (10% Co) samples using alternatives to the two step etching process previously discussed. This research was aimed at providing a better etchant than Murakami solution to study the grain interfaces of carbide substrates. When grains in the metal matrix were very small, it was difficult to observe the microstructure, thus etching was performed to create distinction. In past studies, Murakami solution showed indistinguishable grain boundaries in SEM images. The WC-Co substrate samples used in this experiment were created by isostatically pressing a powder mix under 200 MPa of pressure. The substrates were then sintered at 1375°C for 1 hour under vacuum using a graphite furnace. Each sample was then polished to achieve a 1 μm surface finish. The first alternative etching process was tested using a reagent of boiling H_2O diluted HCl for a 12 hour submersion. The researcher discovered that when the WC-Co substrates were boiled in HCl, the Co particles were dissolved. The interface between WC and Co became visible, but the WC grain boundaries were not revealed. This method was undesirable because it required a long soak time to break down the Co particles and expose the WC grains. The second alternative method involved soaking in an etchant composed of 90% H_2O_2 and 10% HNO_3 at 60°C for 12 minutes. This method dissolved the Co particles much faster than the first. Unlike the boiling HCl, the new etchant was able to dissolve WC particles as well, which allowed for the WC-Co interface and WC grain boundaries to become visible.

2.3. Ultrasonic Cleaning

Ultrasonic pulsation is commonly used for cleaning applications. In a reagent bath, ultrasonic waves help to continuously flush the cleaning solution from the surface of a part, allowing fresh solvent to stay in contact with the workpiece. This same phenomenon can be applied in etching processes [30] such that uncontaminated etchant solution is constantly in contact with the surface of the workpiece. The second aspect of ultrasonic pulsation is the formation of cavitation bubbles on the surface of the workpiece. When bubbles grow and become unstable they burst, causing a pressure wave to propagate throughout the reagent and remove loosely adhered contaminants.

Brujan et al. [33] studied the bursting pressure of cavitation bubbles formed by ultrasonic pulsation. Shock waves emitted by the collapse of cavitation bubbles on the rigid wall

of a workpiece had the largest damage potential. Brujan used a sinusoidal ultrasonic pulser at 1.08 MHz for 30 cycles paired with a 60 dB radio frequency amplifier to generate ultrasonic waves. An aluminum block was used as the solid wall workpiece. During cavitation, when bubbles expanded to their maximum volume, they violently collapsed creating a shock wave of pressure. This shock wave was captured using an IMACON 200 high speed camera with a 200 millions/s framing rate at 5 ns exposure time. Images on the fluorescent screen were then recorded with a 4800 x 3920 pixel array ICCD camera system and digitized to 12-bit resolution. The shock wave velocity, captured by high speed imaging, was used to calculate the pressure values along the front of the shock wave. At a distance of 68 μm from the bubble wall, the maximum shock wave pressure was measured to be 1.3 ± 0.3 GPa. Extrapolation of the data showed that pressures on the wall of the workpiece were as high as 7.7 ± 1.6 GPa. These results were in line with the work of Pecha and Gompf [34]. WC-Co has a compressive strength of 3347-6833 MPa and a tensile strength of 370-530 MPa [35]. These values are at least one order of magnitude lower than the minimum bursting pressure of cavitation bubbles.

2.4. Summary of Literature Review and Research Gap

Previous MQL research has focused on the effect of channel geometry, lubricant type, and aerosol flow parameters on mist characteristics, and machining results using internal and external delivery methods. Past studies have shown that in both external and internal MQL high air pressure decreases the microdroplet size. Low viscosity lubricants have smaller contact angles, increasing wettability and machining quality. There has been little research into how channel roughness affects the droplet distributions and subsequent machining in drilling operations.

Chemical etching of WC-Co substrates has been studied to roughen surfaces for better adhesion. Efforts have been made as well to study microstructure and the interface between WC grains and the Co binder. The following section presents the experimental work and computer simulations on how surface finish of MQL nozzles affect droplet size, and proposes a technique to modify nozzle surface texture.

3. EXPERIMENTS*

3.1. MQL Droplet Characterization

3.1.1. Equipment

The MQL system (Figure 5) consisted of the Unist Coolubricator (Michigan, USA) (D) with three connecting test tips at the output nozzle (E). The system was connected to a compressed air supply through an air regulator (A), air flow meter (B), and pressure gauge (C). A paper grid stored under a 236 x 182 mm glass picture frame (F) was used to collect the micro droplets distributed by the MQL system. A jack plate (G) was used to adjust the distance between the test tip and glass plate.

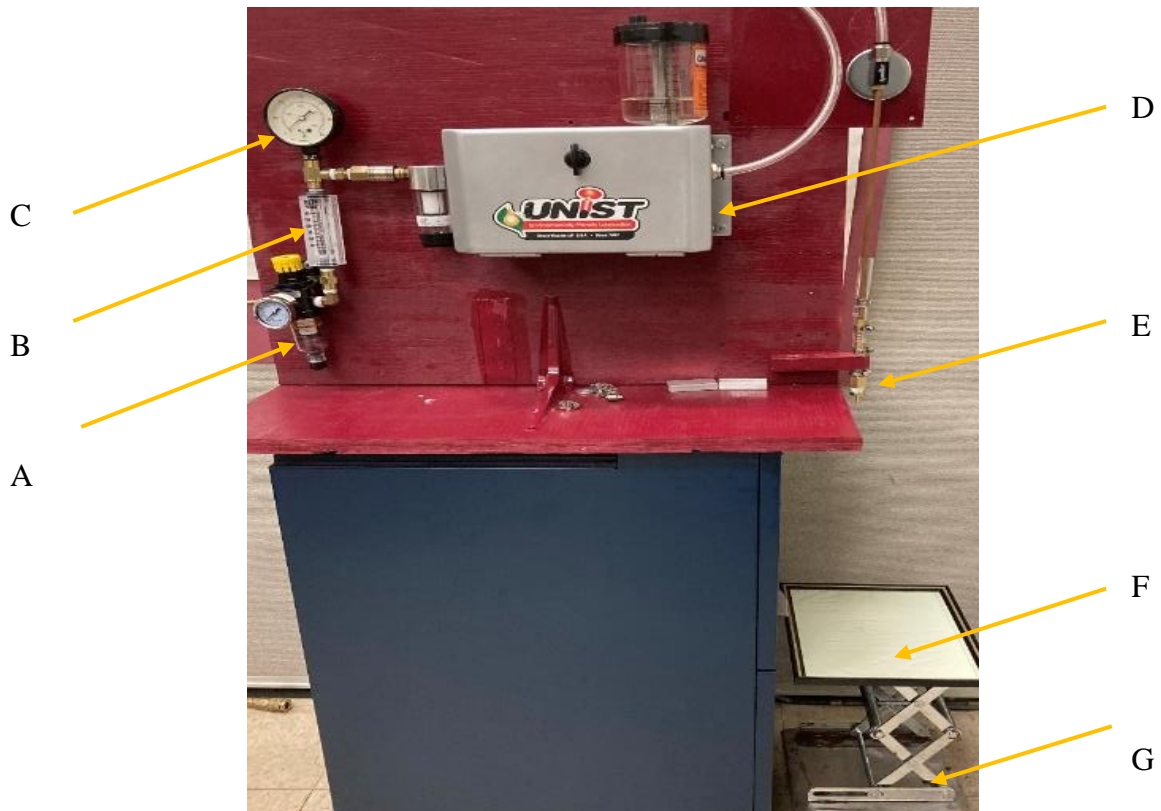
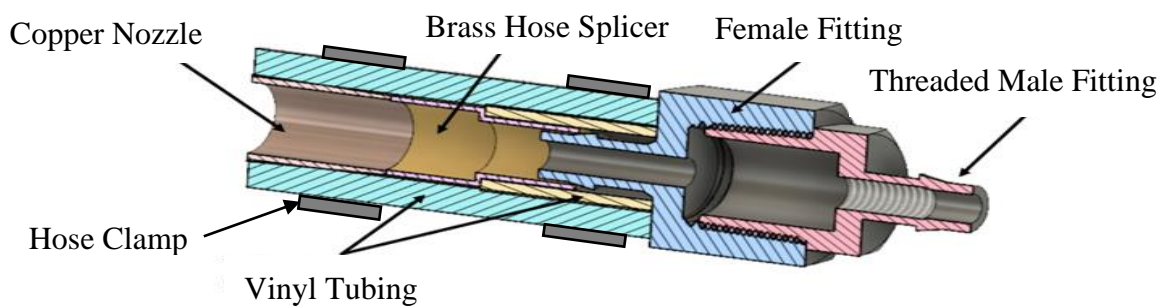


Figure 5. Micro droplet system. A: Air regulator, B: air flow meter, C: pressure gauge, D: MQL Unist Coolubricator, E: output nozzle, F: drop collection plate, and G: jack plate. (B)

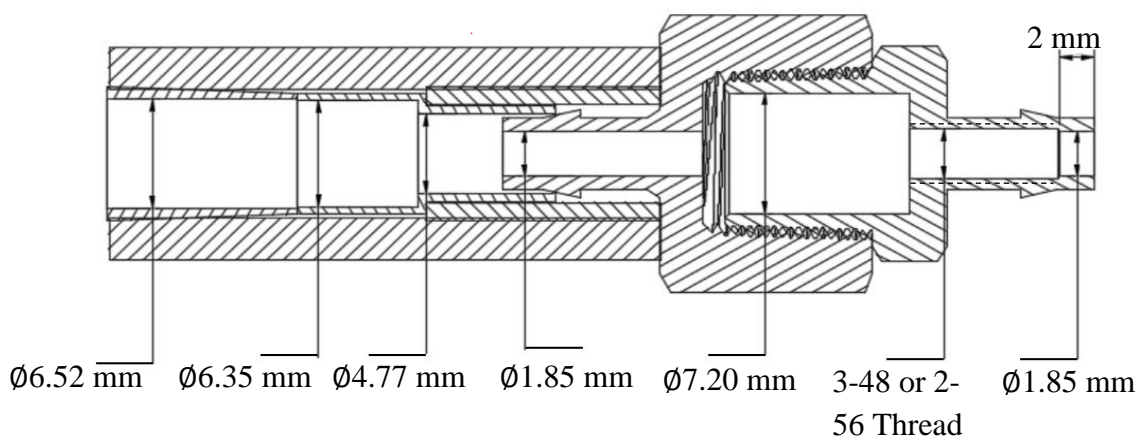
*Reprinted with permission from “Effect of Channel Roughness on Micro-Droplet Distribution in Internal Minimum Quantity Lubrication” Craig M., Raval J., Tai B., Patterson A., and Hung W., Dynamics, vol. 2, no. 4, pp. 336–355, by the authors 2022.

Figure 6 shows detailed schematics of how the Unist Coolubricator copper nozzle was mounted to the test tips. A brass hose splicer was connected to the copper nozzle and 3.175 mm (1/8-in) x 6.25 mm (1/4-in) diameter Barbed Barb x MIP Adapter Female Fitting using Ø6.25 mm vinyl tubing. The tubing was wrapped in Ø9.525 mm (0.375 in) vinyl tubing to add rigidity when securing the hose clamps. The smooth, partially threaded, and threaded 3.175 mm x 6.35 mm diameter Barbed Barb x MIP Adapter Male Fittings were screwed into the female fitting.

Figure 7 shows a polar coordinate layout of the collection grid used to acquire data pertaining to the droplet distribution as a function of radial distance. Due to the conical shape of exit aerosol mixture from a channel, eight different zones surrounding the nozzle were used to capture most of the droplets. The 8 locations were used to collect images at 5 different distances from the outlet tip (0 mm, 39.6 mm, 50.8 mm, 61 mm, 93.4 mm). Before each test, the outlet tip was centered above location 5, making it the origin point.



(A)



(B)

Figure 6. Test Tip Assembly and Dimensions

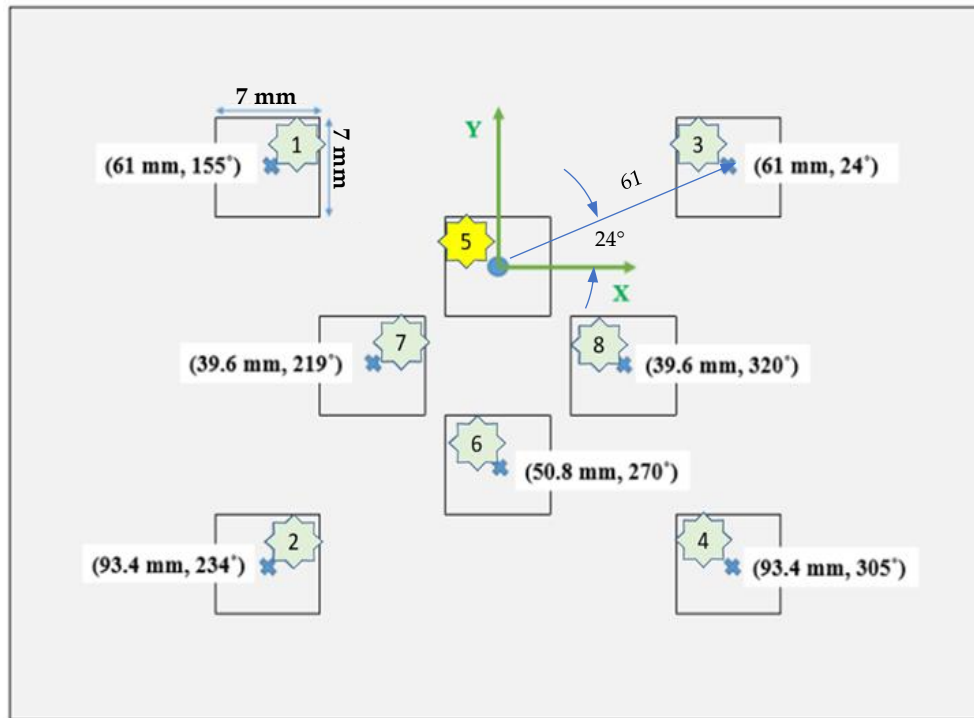


Figure 7. Polar Coordinate Representation of Collection Zones. The Origin is at the Center of the Tip Projection at Location 5

3.1.2. Materials

Three channel finishes were achieved by modifying Barbed MIP adapters. A smooth channel was tested using an as drilled fitting. A PT channel was made using a #2-56 tap ($\varnothing 2.18$ mm) to create internal threads. The major diameter cut only partial threads in the channel. The FT channel was threaded with a #3-48 tap ($\varnothing 2.51$ mm). This tap cut fully into the channel, creating deeper threads and a rougher internal surface finish. Past studies showed that threading from the entrance to the exit of the tip caused lubricant build up at the exit. Because of this, for both the PT and FT channels, the threads were not tapped all the way through to the tip. Approximately 2 mm of the channel was left untapped to decrease the amount of lubricant coalescence at the outlet of the nozzle. Both Coolube 2210A1 and Castrol Hyspray A1536 were tested. The properties of each lubricant, gathered from manufacturer data sheets and the work of Patil et al. [26], are shown in Table 6.

Table 6. Tested Lubricants and Properties. Adapted From [26]

Properties	Coolube 2210A1	Castrol Hyspray A1536
Oil Type	Fatty Acid and Alcohol Mixture	Vegetable
Kinematic viscosity at 40°C (mm ² /s)	14.5	28
Kinematic viscosity at 100°C (SUS)	Not Available	148
Flashpoint (°C)	93	194
Density (kg/L)	0.82-0.92 at 60°C	0.838 at 20°C
Thermal conductivity at 40°C (W/m°K)	Not Available	0.1593
Contact angle on glass	6°	22°
Solubility	Hydrocarbons, alcohols	Insoluble in water

The tip to grid distance was optimized at 356 mm to avoid lubricant coalescence on the collection grid. This distance was used for every test.

3.1.3. Methods

The fixed and variable parameters used for micro droplet collection are shown in Table 7A and 7B respectively. The following procedure was used for micro droplet collection:

1. The Unist Coolubricator was set to 40 strokes/min lubricant delivery.
2. A compressed air line was connected to the system and the inlet pressure was set to 690 kPa (100 psi).
3. The smooth, PT, or FT tip was connected to the system.
4. The tip to grid distance was set to 356 mm (14 inches).
5. A bubble level was used to ensure parallelism of the tip and collection grid.

6. The glass plate was cleaned using glass cleaner then acetone. A weight was hung from the system outlet tip to position it above location 5 on the collection grid.
7. The system was turned on and the tip was covered for 30 seconds to allow for lubrication flow to start.
8. The blockade was removed. After 1 second the tip was covered to stop the collection period.
9. The grid was transferred to the Olympus STM6 microscope (Japan) for image capturing. One 7 x 7mm² microscopic image of droplet distribution was captured at the center of each zone seen in Figure 4. The images were then processed and the resultant droplet diameters were captured using Adobe Photoshop and ImageJ respectively.
10. Steps 1-9 were repeated for each channel roughness using Coolube and Castrol lubricants.

Table 7. MQL Droplet Collection Parameters

A. Fixed Parameters						
Parameter	Tip to Grid Distance	Air Flow Rate	Air Pres- sure	Pump Frequency	Collection Time	Lubricant Quantity
Set Point	356 mm (14 in)	0.566 m ³ /hr	690 kPa (100psi)	40 strokes/ min	1 second	60 mL/hr
B. Variable Parameters						
Parameter	Channel Roughness			Lubricant Type		
Set Point	Smooth, Partially Threaded, Fully Threaded			Coolube vs. Castrol		

Nonparametric statistical analysis was conducted to further analyze the results of the droplet distributions. The experimental design for this analysis is shown in Table 8.

Table 8. MQL Droplet Characterization Experimental Design

	A: Lubricant Type	B: Radial Distance (mm)	C: Channel Roughness
1	Coolube	0	Smooth
2	Castrol	0	Smooth
3	Coolube	39.6	Smooth
4	Castrol	39.6	Smooth
5	Coolube	50.8	Smooth
6	Castrol	50.8	Smooth
7	Coolube	61	Smooth
8	Castrol	61	Smooth
9	Coolube	93.4	Smooth
10	Castrol	93.4	Smooth
11	Coolube	0	PT
12	Castrol	0	PT
13	Coolube	39.6	PT
14	Castrol	39.6	PT
15	Coolube	50.8	PT
16	Castrol	50.8	PT
17	Coolube	61	PT
18	Castrol	61	PT
19	Coolube	93.4	PT
20	Castrol	93.4	PT
21	Coolube	0	FT
22	Castrol	0	FT
23	Coolube	39.6	FT
24	Castrol	39.6	FT
25	Coolube	50.8	FT
26	Castrol	50.8	FT
27	Coolube	61	FT
28	Castrol	61	FT
29	Coolube	93.4	FT
30	Castrol	93.4	FT

3.2. MQL Lubricant Flow Simulations

Simulations of the MQL flow within each channel were conducted to analyze the experimental based results. ANSYS Fluent 2020 software was used along with the boundary conditions listed in Table 9.

Table 9. MQL Simulation Boundary Conditions

Boundary Condition	Total Inlet Pressure (psig)	Static Inlet Pressure (psig)	Outlet Pressure (psig)	Inlet Temperature (K)	Outlet Temperature (K)	Primary Phase
Specification	60	25	0	300	300	Air

3.3. Chemical Etching of WC-CO

3.3.1. Equipment



Figure 8. Chemical Etching Setup. Where, A: Hot Plate, B: Glass Pan, C: 250 mL Beaker, D: Tool Hanger, E: Jack Plate, F: Ultrasonic Pulser, G: Chilled Bath

Figure 8 shows the system used for chemical etching of the WC-Co samples. A Lab Depot Inc. hot plate (A) was used to heat the reagent bath. A series of water baths were used to allow for ultrasonic waves to be transmitted through the reagent while keeping the 50 kHz frequency ultrasonic pulser (F) within its operating temperature range and out of contact with

the etching solution. A large glass pan (B) was used to contain the heated water bath. A 250 mL beaker (C) was placed in the hot water bath, centered over the hot plate. This beaker contained the etching solution. Nylon fishing line was used to attach a 6.35 mm x 6.35 mm dowel rod and binder clip, creating the tool insert hanger (D). The line was spooled around the dowel to control the height of the hanger, dictating the depth in which the inserts were submerged in the reagent. To isolate the ultrasonic pulser away from the hot plate, a jack plate (E) was used such that the large glass pan could be offset to the side of the heated surface. An ice-chilled water bath (G) was used to reduce the temperature of the water surrounding the ultrasonic pulser.

3.3.2. Materials

The etchant developed by Jung et al. [32] was used in this experiment to characterize the effect of etching on surface roughness. This solution was created using a 9:1 ratio of 34% hydrogen peroxide (H_2O_2) and nitric acid (HNO_3) respectively, heated to 60°C . For ease of mixing, the molar ratio was converted into a mass ratio such that each chemical could be weighed for quick measuring purposes. Hydrogen peroxide and nitric acid have molar masses of 34.01468g/mol and 63.01284g/mol respectively. The conversion was completed as follows:

$$9 \text{ mol } \text{H}_2\text{O}_2 \times 34.01468\text{g/mol} = 306.13212\text{g of } \text{H}_2\text{O}_2$$

$$1 \text{ mol } \text{HNO}_3 \times 63.01284\text{g/mol} = 63.01284\text{g of } \text{HNO}_3$$

Since only small amounts of reagent were used for each trial, these values were reduced by a factor of 20. The mixture used for each experiment was effectively measured to be a ratio of 15.30g H_2O_2 and 3.15g HNO_3 . The mass of each solution was measured using an AWS LB-1000 compact scale.

The WC-Co workpieces used in the etching experiment were K20 TPG 433 C2 triangular milling inserts (6% Co) (Pennsylvania, USA). These inserts were chosen because they have similar composition to the WC-Co internal MQL drill bits used in industry.

3.3.3. Methods

1. The fume hood fan and light were turned on.
2. The jack plate height was set such that the static ultrasonic bath dish was supported level between it and the hot plate.
3. The ultrasonic pulser was placed in the ice bath. The ice bath dish was set in the static bath centered above the jack plate. The ice bath was filled such that the ultrasonic pulser was fully submerged.
4. A 250 mL beaker was placed in the static bath centered above the hot plate. The static bath was filled until approximately the 50 mL mark on the beaker was submerged.
5. The 90% H₂O₂ 10% HNO₃ solution was mixed by adding 3.15g of HNO₃ to 15.31g H₂O₂. The mixture was then added to the 250 mL beaker.
6. The hot plate was turned on high (setting 9) to allow the reagent to heat until it reached 55°C. The heat was then lowered to setting 4 such that the reagent could stabilize at 60°C.
7. The tool insert was cleaned using isopropyl alcohol and dried with paper towel. After cleaning, the insert was secured in the tool hanger binder clip.
8. In trials that utilized the ultrasonic pulser, the run time was set to 900 seconds and the device was turned on. Note: The timer had to be reset during the 20 minute trials.
9. The tool hanger was slowly unspooled and the tool insert was lowered into the 250 mL beaker until the tip was submerged in the reagent. The tool hanger was gently agitated by hand until the etching run time concluded.
10. After the tool was removed from the reagent it was rinsed with water.
11. The used reagent was disposed of in a safe container. The 250 mL beaker was rinsed with water and dried using compressed air.
12. Steps 4-11 were repeated for the remaining trials. The ultrasonic pulser ice bath was replenished as needed.

13. After the etching experiment the tool inserts were cleaned using a 10 minute isopropyl alcohol bath. Images were captured on the Alicona Infinite Focus G4 measurement system (Austria). Ra and Sa roughness measurements were taken on both pre and post-etched surfaces.

14. Before SEM and optical images were captured on the TESCAN Vega3 (Czech Republic) and Olympus STM6 microscopes respectively, samples 1 and 3 were cleaned using a 30 minute ultrasonically pulsed acetone bath. The samples were allowed to dry in a dry box for 2 hours before being transported to the microscope.

The initial test was conducted using hand agitation (HA) for 12 minutes. The tool insert was viewed under an optical microscope to analyze the extent of etching. It was determined that the as purchased grinding marks were still visible, and because of this the experiment was run again using a 20 minute etching time. After 20 minutes the grinding marks were no longer visible. The 12 and 20 minute tests were then run using a combination of hand agitation and ultrasonic pulsation (HA + US). The 12 minute HA + US run etched enough material such that the grinding marks were no longer visible. Because of this, a 5 minute etching time with HA + US was run to analyze the results. A second trial was then conducted for each experiment described above.

3.4. Metrology

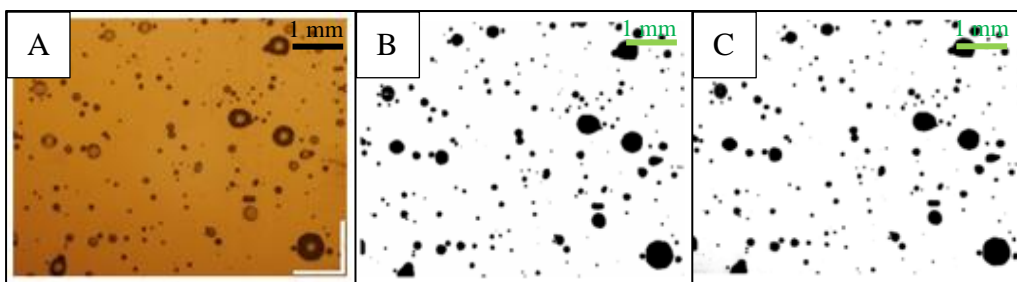


Figure 9. (A) Microscope Captured (B) Adobe Photoshopped (C) ImageJ Processed

An Olympus STM6 microscope was used to collect images of the micro droplet distribution seen in each test (Figure 9A). Adobe Photoshop v 22.5.1 was used to convert the microscope images to grayscale to increase the contrast between the droplets and background (Figure 9B). This process is detailed in Appendix B1. ImageJ 1.52a was used to adjust the image thresholds and capture the projected area of the microdroplets (Figure 9C). This process is detailed in Appendix B2.

The resultant surface roughness measurements before and after etching were captured using an Alicona Infinite Focus G4 measurement system. The system was calibrated using a 20x objective lens and Mitutoyo standard 178-602. The upper wavelength filter cutoff was set to 470 μm . Surface roughness values were taken using both Ra and Sa measurements. 4 total measurements were taken on the top (polished side) and bottom of the tool inserts. On both sides a measurement was made in the center and at the edge of the etched and non-etched locations. Because Ra values are line based, an average of 5 measurements was taken at each location. Ra measurements were recorded using a 0.5 mm line and Sa measurements were recorded using a 0.25 mm x 0.25 mm area.

A TESCAN Vega3 microscope was used to capture images of the grain structure amongst the surface of the polished side of the tool inserts. This allowed for comparison of the pre and post-etched surfaces of substrates tested using HA and HA + US methods. Figure 10 shows the tooling inserts loaded on the table inside of the microscope's vacuum chamber.

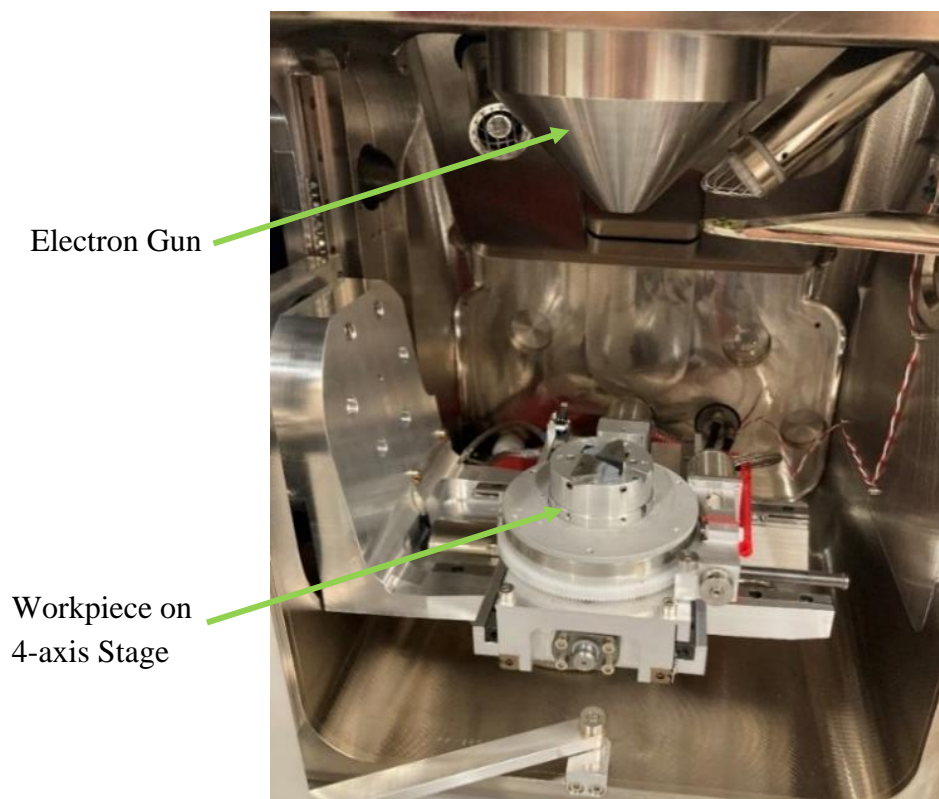


Figure 10. Scanning Electron Microscope Vacuum Chamber

An Olympus STM6 microscope was used to capture images at 50x magnification such that the results of the SEM imaging could be supported. Helicon Focus 8 software was used

to focus stack microscope images of the etched tool inserts. This process is detailed in Appendix D.

Throughout the etching experiment a Raytek Raynger ST20 Pro Standard Noncontact Thermometer was used to measure the temperature of the reagent bath.

4. RESULTS AND DISCUSSION*

4.1. MQL Droplet Characterization

Figure 11 shows resultant droplets for both Coolube and Castrol lubricants using each channel roughness. Some droplets were too small for the ImageJ software to capture ($< 1.6 \mu\text{m}$ projected diameter), and were not used in analysis. Due to lubricant coalescence, a few occurrences of combined droplets occurred. To reduce skew in the distributions, large droplets ($> 200 \mu\text{m}$ projected diameter) were excluded from the analysis.

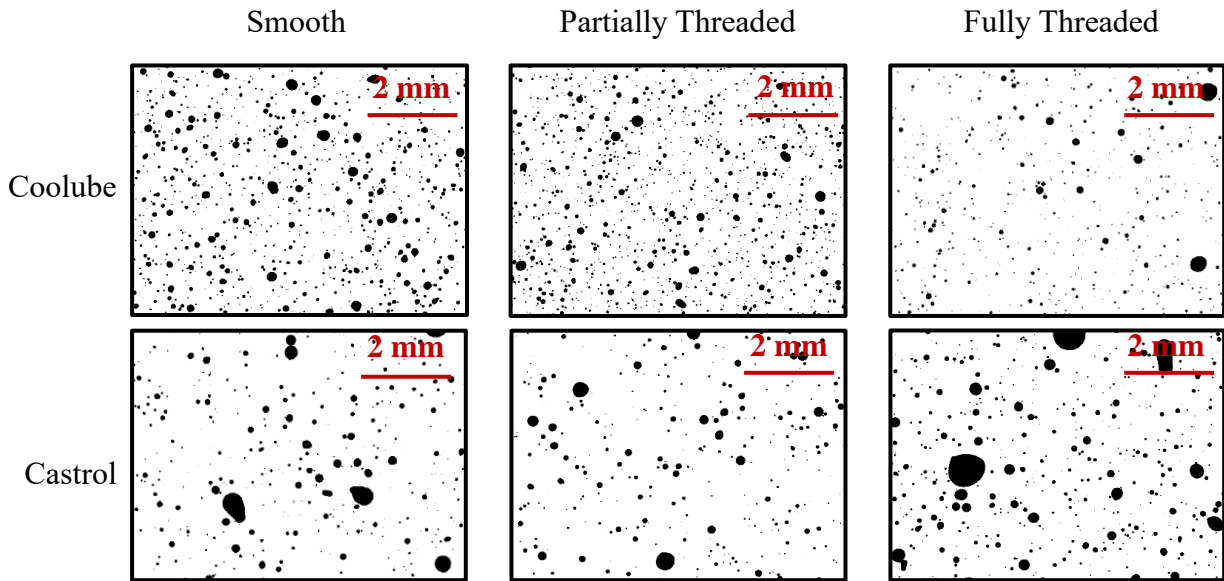


Figure 11. Resultant Microdroplet Images for Coolube and Castrol Lubricant at Location 7 (39.6 mm, 219°) and 690 kPa

The projected droplet areas A were calculated by ImageJ using the image pixels. Assuming perfect circles of projected droplets, the projected diameter P was calculated using equation (1):

$$P = 2 \left(\frac{A}{\pi} \right)^{1/2} \quad (1)$$

*Reprinted with permission from “Effect of Channel Roughness on Micro-Droplet Distribution in Internal Minimum Quantity Lubrication” Craig M., Raval J., Tai B., Patterson A., and Hung W., Dynamics, vol. 2, no. 4, pp. 336–355, by the authors 2022.

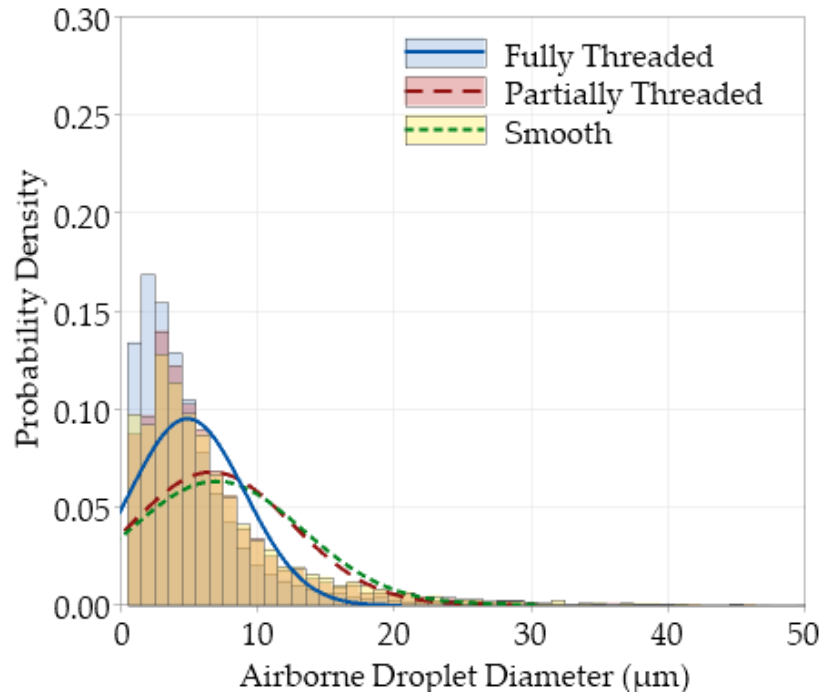
Knowing the respective contact angle θ , and projected size P , the droplet volume V was calculated from equation (2), where $K = 1$ if $\theta < 90^\circ$ and $K = 0$ if $\theta > 90^\circ$:

$$\frac{P^3}{V} = \left(\frac{24}{\pi}\right) \left[\frac{(1 - K \cos^2 \theta)^{3/2}}{2 - 3 \cos \theta + \cos^3 \theta} \right] \quad (2)$$

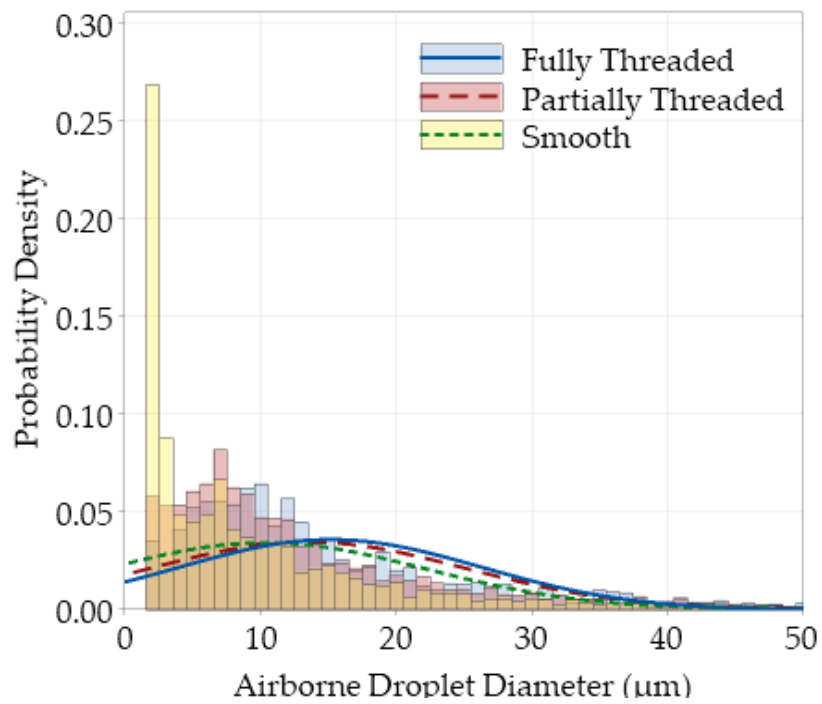
Assuming no evaporation during flight, no splashing when impacting the glass plate, and no droplet coalescence on the glass plate, an airborne droplet would have the same volume as that on the plate. Its airborne diameter d was simply:

$$d = \left(\frac{6V}{\pi}\right)^{\frac{1}{3}} \quad (3)$$

Equations 1-3 were combined and simplified to solve for an airborne droplet diameter constant, N , by which the projected diameters of each lubricant were multiplied to calculate the airborne droplet diameter d . For Coolube and Castrol oil, N was found to be 0.2699 and 0.4195 respectively.



(A) Coolube



(B) Castrol

Figure 12. Airborne Droplet Diameter Distribution for Different Lubricants

Table 10. Statistical Analysis of Airborne Droplet Diameters.

	Coolube (14.5 mm ² /s viscosity)				Castrol (28.0 mm ² /s viscosity)			
Channel surface	Mean (μm)	Standard Deviation (μm)	Standard Error (μm)	Droplet count	Mean (μm)	Standard Deviation (μm)	Standard Error (μm)	Droplet count
Fully threaded	4.93	4.20	0.05	8445	15.15	11.12	0.25	1905
Partially threaded	6.71	5.90	0.07	6988	13.53	11.64	0.26	2033
Smooth	7.05	6.33	0.08	6132	10.41	11.75	0.22	2744

Figure 12 shows the distribution of drop size as a probability density (frequency of occurrence), and the numeric results of these distributions are shown in Table 10 to compare the effects of channel roughness on droplet quality and quantity. Opposite trends were found for lubricants Coolube and Castrol:

1. The low viscous Coolube lubricant was easily broken into smaller droplets. The ability to self-divide into smaller droplets was enhanced by a rougher surface as evidenced with the change from smooth to partially threaded and fully threaded channels.
2. The high viscous Castrol lubricant showed the opposite trend. Higher viscosity forced lubricant droplets to adhere to the channel wall, forming larger droplet sizes. A rougher surface would promote this characteristic, i.e., more lubricant adhering to the channel wall and less number of airborne droplets.
3. Standard deviation showed the spread of droplet size amongst the mean. Due to large outlying droplets, the standard deviation was high for each trial. Standard error was calculated by dividing the standard deviation of the airborne droplet diameter by the square root of the droplet count, and normalized the standard deviation for a more meaningful representation of uncertainty throughout the experiment. This was used

for a better comparison of the droplet size deviation with respect to the large difference in droplet count between Coolube and Castrol lubricant. The standard error was much lower in Coolube lubricant trials, showing that it was more uniformly distributed in small droplets. Castrol lubricant, with a higher standard error, showed more deviance from the average droplet size due to large droplets and coalescence.

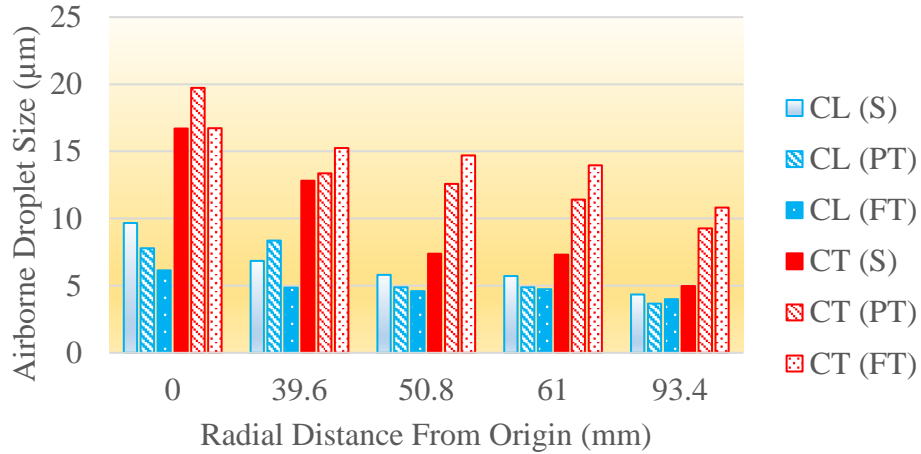
The low viscous Coolube lubricant allowed the desirable and smaller droplet size with increasing channel surface roughness. Such results were confirmed with another study where airborne droplets were collected through a rough 3D printed ABS channel and through an acetone polished ABS channel [3]. In a subsequent section, the computer simulation of MQL mixture through different channels further explains the effect of lubricant viscosity on quality of MQL mixture.

The MQL mixture is characterized by drop size, speed, and its distribution in a flow.

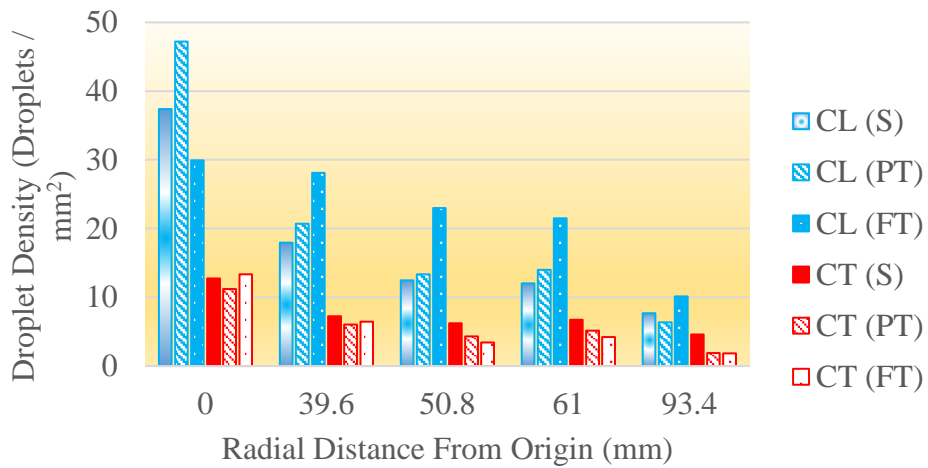
Let:

$$\text{Droplet density (drops / mm}^2\text{)} = \frac{\text{Number of droplets}}{\text{Collection area (mm}^2\text{)}} \quad (4)$$

Figure 13 shows the airborne droplet diameter (calculated using equations 1-3) and droplet density as a function of radial distance for Coolube and Castrol. Droplet density is defined as the number of droplets per mm^2 , and was calculated by dividing the droplet count in each image by the image area of 49 mm^2 .



(A)



(B)

Figure 13. Effect of Radial Distance and Surface Roughness on Droplet Quality of Coolube (CL) and Castrol (CT). S: Smooth, PT: Partially Threaded, FT: Fully Threaded

Figure 13A and Figure 13B show negative trends. The combination of these plots summarized the dispersion behavior throughout this experiment. Assuming negligible evaporation of airborne droplets and negligible coalescence of these droplets, the dispersion is due to cone shaped air flow at the exit. The experimental data showed the following:

1. Droplet dispersion: High droplet density was found directly below the nozzle since compressed air exited within a cone shape and diverged away from the tip. Higher central air velocity constrained the droplets near the central axis of the cone and deposited most droplets in the central zone #5.

2. Airborne drop size: The data showed drop size was larger at the central zone #5 compared to other zones. A large droplet with heavy mass and inertia would travel straight out of the nozzle and have less tendency to deviate from a flight path due to minor turbulence.

3. Effect of Lubricant Type: The Coolube lubricant, with viscosity of 14.5 mm²/s compared to 28 mm²/s of Castrol Lubricant (Table 6), would easily break down into smaller droplets to form mist with smaller airborne drop size and higher droplet density. This reasoning also agrees with the relationship of contact angle and surface tension in the Gibbs equation [37]:

$$\cos\theta = \frac{\gamma_{SG}-\gamma_{SL}}{\gamma_{LG}} + \left(\frac{K}{\gamma_{LG}}\right)\left(\frac{1}{a}\right) \quad (5)$$

Where,

θ : contact angle

γ_{SG} : surface tension of solid relative to gas

γ_{SL} : surface tension of solid relative to liquid

γ_{LG} : surface tension of liquid relative to gas

K : line tension

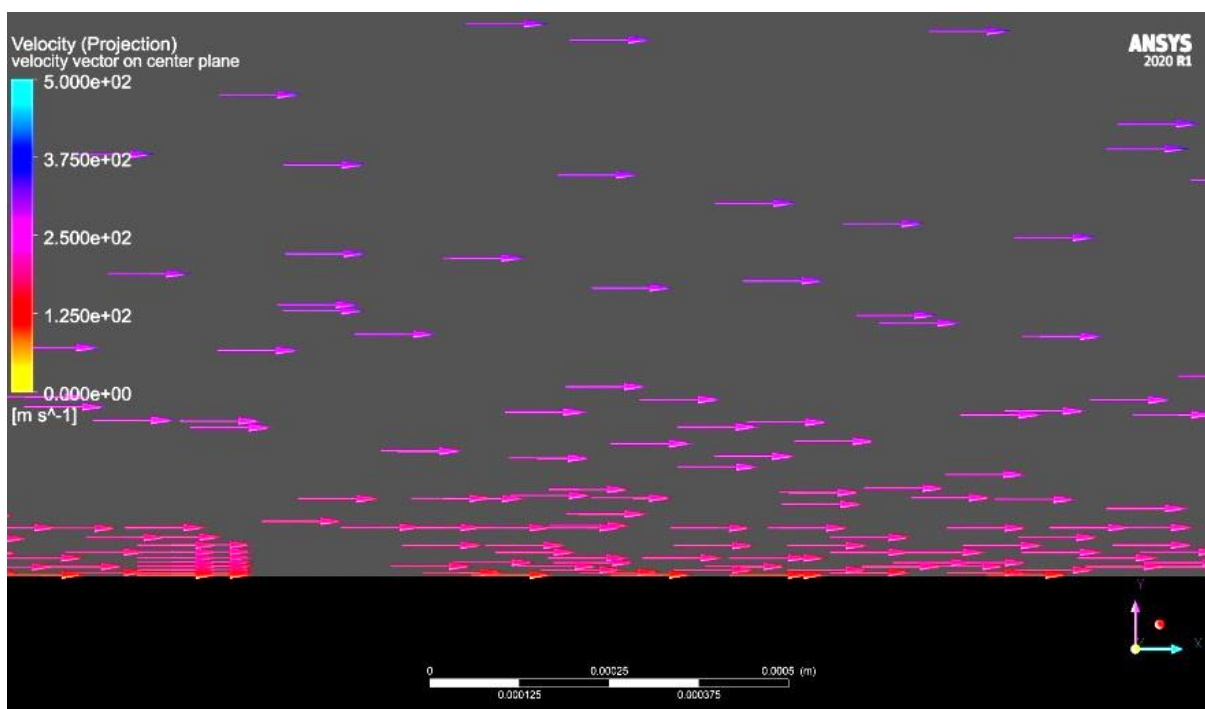
a : droplet radius

Table 6 tabulates the smaller contact angle of Coolube lubricant relative to lubricant Castrol. Equation (5) suggests that a liquid with smaller contact angle would form a smaller droplet, thus, having the smaller radius a . Patil et al. [26] used a high speed video camera and confirmed the smaller airborne drop size of Coolube lubricant compared to that from Castrol at different air pressure levels. It is important to note that the effect of radial distance is more suited toward external MQL, where the aerosol mixture is sprayed from a distance. In this application, the best trajectory of droplet flow would be achieved by aiming the nozzle directly at the cutting zone, and keeping the axial distance between the tip and workpiece small. In internal MQL, the outlet of lubricant delivery channels is very close to the tool-chip interface. Because of this, the radial distance is close to 0 mm.

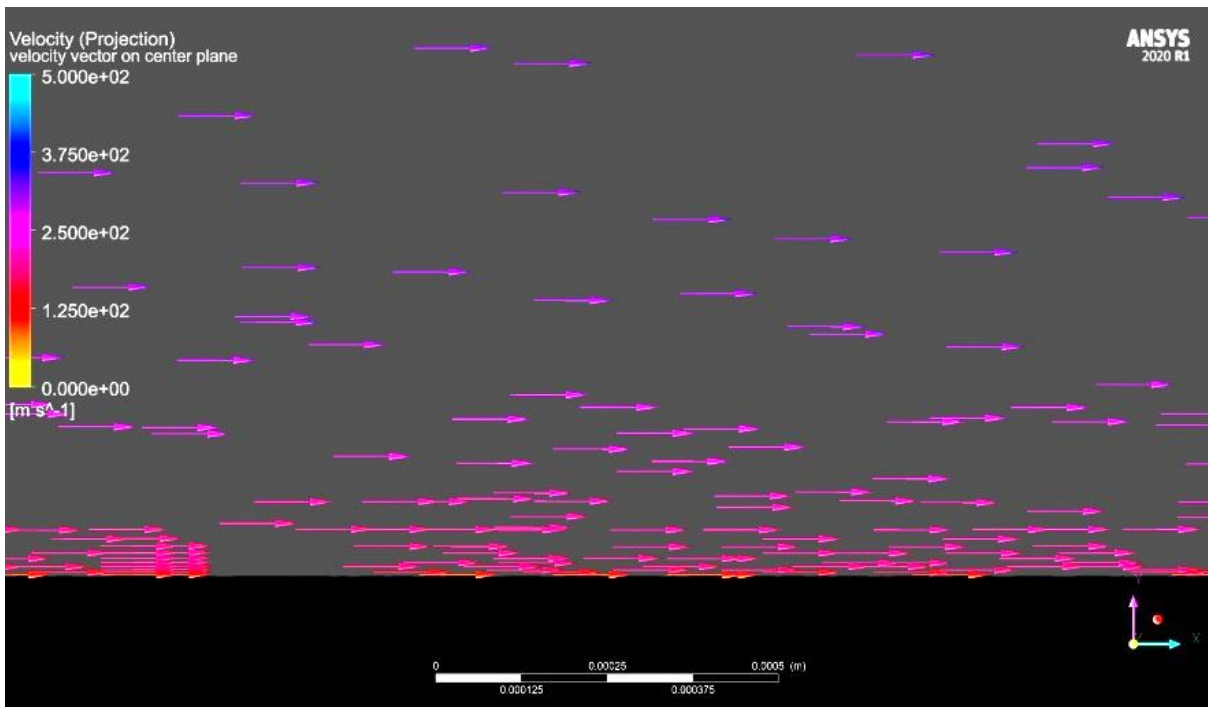
The experimental results from this study agreed with information from published literature. The results of the droplet characterization experiment were consistent with the works of Patil et al. [26], who also tested both Coolube and Castrol, and concluded that the combination of low viscous Coolube lubricant and high air pressure resulted in smaller airborne droplets. Tai et al. [16] tested esters, naturally derived synthetics, vegetable based lubricants, and fatty oils and showed differing results as an opposite trend in viscosity and droplet size was observed. The combination of the trends in Figures 13A and 13B is supported by the work of Park et al. [38], who studied wetting area as a function of radial distance from the collection zone to the MQL nozzle. Wetting area was defined as the total area covered by droplets (mm^2), and was shown to decrease with increasing radial distance. The results of the droplet density and airborne diameter vs. radial distance graphs support this. With an increase in radial distance, the droplet density and airborne droplet size decreased, which corresponded to a smaller droplet coverage area.

4.2. MQL Mixture Flow Simulations

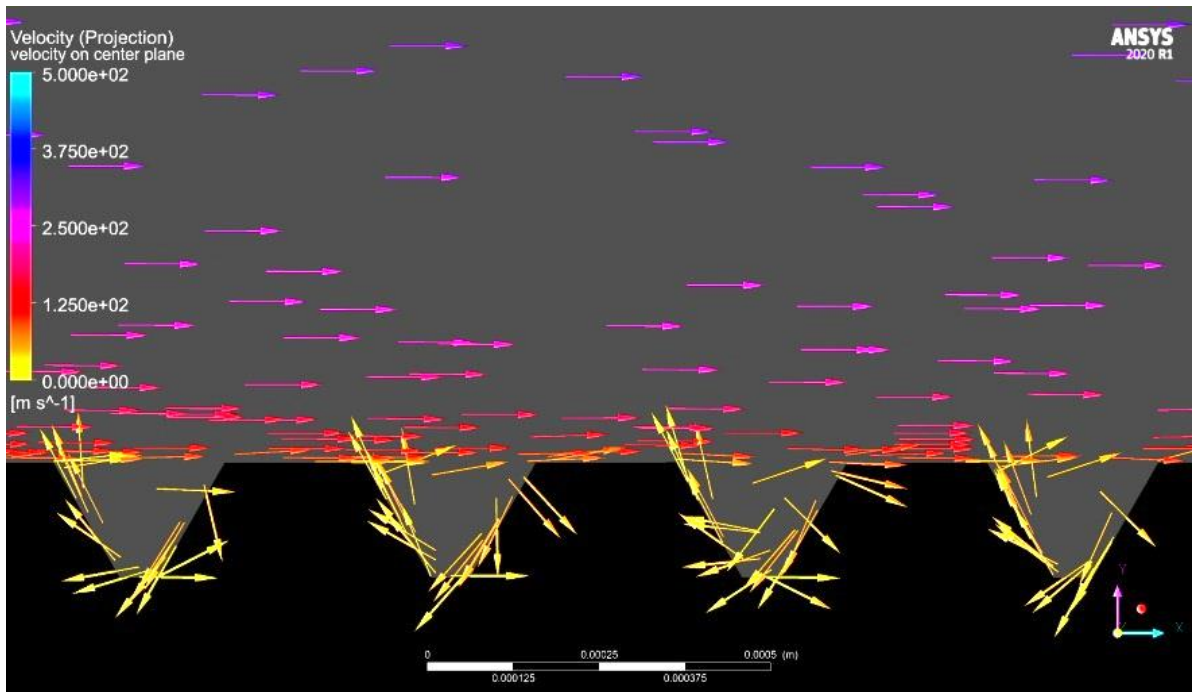
The flow of oil-air mixture in MQL was simulated in a circular channel. Due to the channel symmetry, only a quarter of a channel was shown for each lubricant (Coolube, or Castrol), and different channel roughness (smooth, PT, or FT). Figure 14 shows the velocity of the aerosol mixture near the wall of an internal MQL channel.



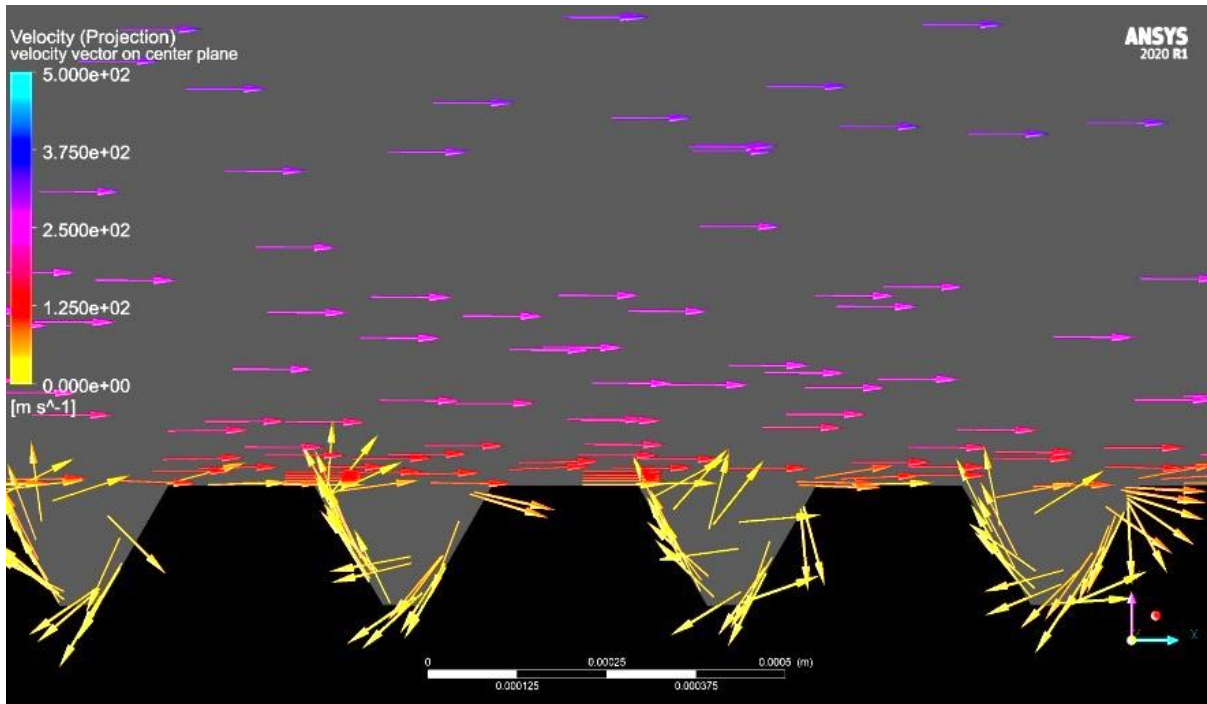
(a) Coolube Lubricant and Air Mixture, Flow Above a Smooth Channel, 410 kPa Pressure.



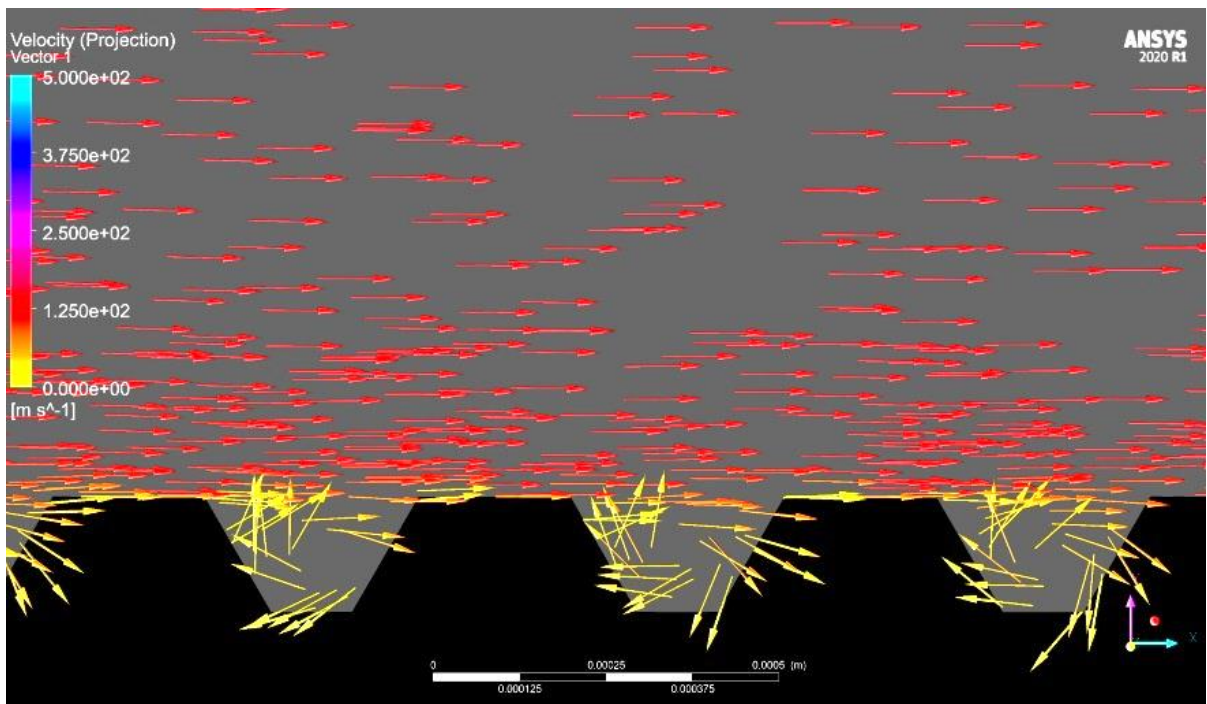
(b) Castrol Lubricant and Air Mixture, Flow Above a Smooth Channel, 410 kPa Pressure.



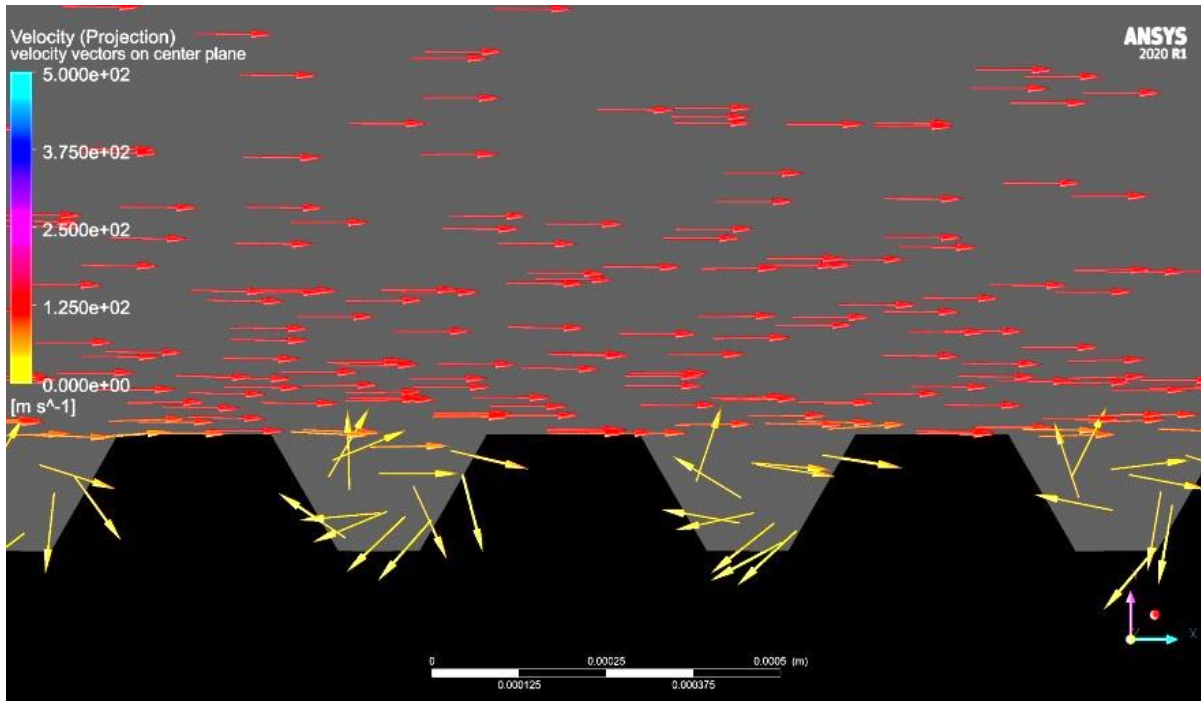
(c) Coolube Lubricant and Air Mixture, Flow Above PT Channel, 410kPa Pressure.



(d) Castrol Lubricant and Air Mixture, Flow Above PT Channel, 410kPa Pressure.



(e) Coolube Lubricant and Air Mixture, Flow Above FT Channel, 410kPa Pressure.



(f) Castrol Lubricant and Air Mixture, Flow Above FT Channel, 410kPa Pressure.

Figure 14. Lubricant Flow Velocity Vectors

The simulation showed the effect of the channel wall roughness on boundary layer and near wall flow pattern:

1. In a smooth channel, the velocity of the air was parallel to the wall. Because of this, the droplets stuck to the wall and it was very difficult for the droplets to reenter the bulk of the fluid (Figure 14a and Figure 14b). Similar results were seen in straight channels tested by Raval et al. [12], as axial air velocity led to lubricant wall adhesion and annular flow.
2. In a partially threaded channel, turbulent flow was seen due to the threaded wall. The thread geometry, typically 60°, allowed air to recirculate back and disrupt the boundary layer (Figure 14c and Figure 14d). This was supported by the results of helical channels [12], which generated secondary vortices that disrupted the boundary layer of lubricant on the channel wall.
3. The effect was more significant in the fully threaded channels (Figure 14e and 14f). The returning air in a threaded portion effectively disrupted the stagnant layer and reintroduced oil droplets back to the main air flow above the threaded wall. As

the result, there was more pressure drop in the fluid and the velocity of the air was lower (approximately 125 m/s) compared to that in a smooth channel (approximately 250 m/s).

The results of the MQL lubricant flow simulation complements the experimental results showing in Figure 11-13. The Coolube lubricant with low viscosity and low surface energy broke up into smaller droplets when flowing through a partially threaded channel, and even finer droplets in fully threaded channel. This is shown by smaller droplets (Figure 13A) and increasing droplet density (Figure 13B). The reason, illustrated with the flow simulation above, was due to the recirculating air flow that disrupted the boundary layer and reintroduced stagnant oil into the downstream flow. The very fine airborne droplets, however, may not have been captured in the experimental study due to possible evaporation or 1 μ m resolution limitation of the optical microscope.

The opposite trend, however, was observed for the higher viscosity and higher surface tension of Castrol lubricant. The oil droplets were larger (Figure 13A), and adhered to the rough surface of the threaded channel. This caused them to not be recirculated into the downstream flow by the very low air velocity within a thread. Therefore, the droplets were larger and less airborne droplets were collected (Figure 13B).

4.3. Nonparametric Statistical Analysis

Analysis was conducted to characterize the effect of each input parameter (lubricant type, radial distance, channel roughness) on the response (airborne droplet size). The experimental design included 30 different combinations of these parameters, shown in Table 4.

A normal probability test (Fig. 15) was used to determine if parametric or nonparametric analysis would best characterize the data set. Parametric analysis, or ANOVA testing, runs on the assumption that the dataset follows a normal distribution. If this assumption is incorrect, ANOVA becomes inaccurate and nonparametric analysis must be conducted. The residual trendline (blue) did not fit to the normal line, and because of this, the assumption of residual normality was not met. This issue could not be corrected by simple transforms or outlier removal, therefore the equal variance assumption was unlikely to be met and ANOVA could not be used validly. Because of this, a nonparametric Kruskal-Wallis test was conducted.

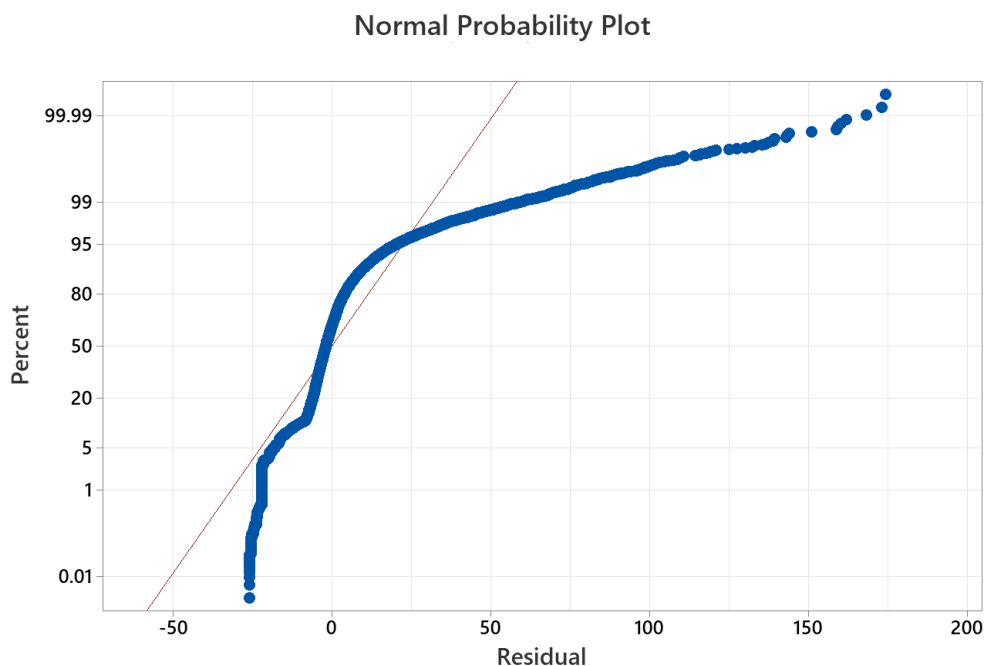


Figure 15. Residuals Compared to Normal Probability Plot

The Kruskal-Wallis tests determined the statistical significance between each individual input parameter and the responsive airborne droplet size. Testing was conducted at a 5% significance level. The results are shown in Table 11.

Table 11. Kruskal-Wallis Test Results

	Lubricant Type	Radial Distance	Channel Roughness
P-Value	< 0.001	< 0.001	< 0.001

The Kruskal-Wallis tests were interpreted as follows: If the P-value returned by the test was less than the significance level (0.05), then the parameter was said to be significant. This meant that statistically, the tested parameter had an effect on the response. In this experiment, the resultant P-values of all three parameters were < 0.001. This showed that lubricant type, radial distance, and channel roughness all had an effect on the resultant airborne droplet size. These relationships were further investigated using main effects and interaction plots (Fig. 16 and 17).

Main Effects Plot for Droplet Diameter

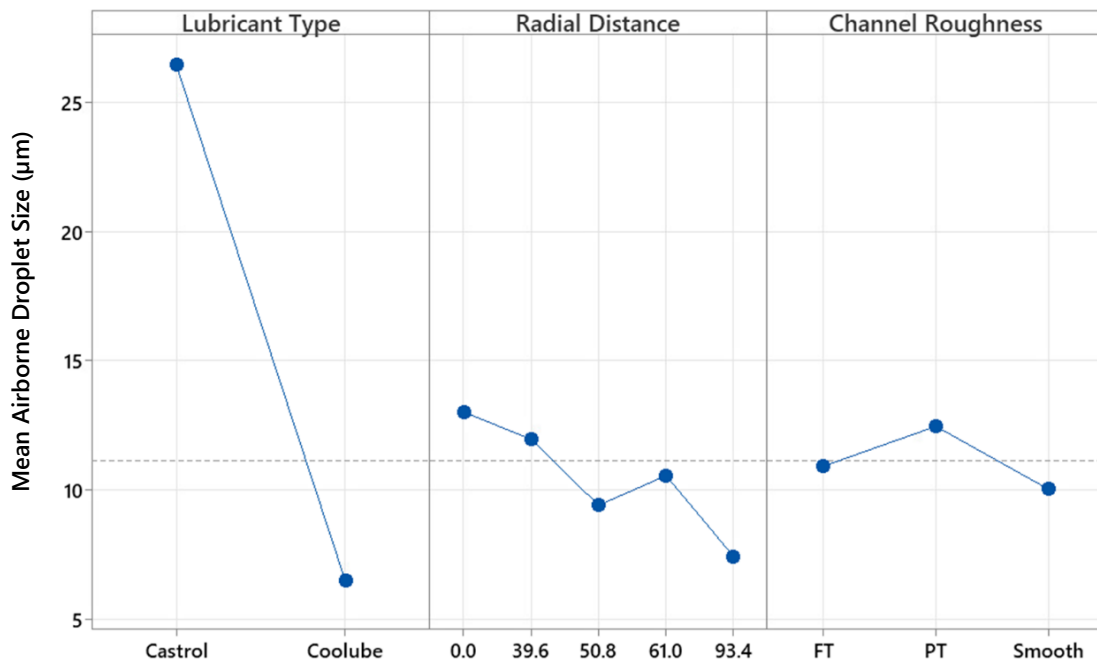


Figure 16. Main Effect of Lubricant Type, Radial Distance, and Channel Roughness on Airborne Droplet Size

In the main effects plot, a steeper slope of a parameter’s trendline symbolized a larger effect on the response. From this, lubricant type had the largest effect on airborne droplet size, followed by radial distance and channel roughness. This aligned with the results shown

in the droplet distributions (Fig. 12) and airborne droplet size vs. radial distance plots (Fig. 13). Coolube lubricant generated overall smaller droplets, and showed a decreasing trend in droplet size with increasing channel roughness. Castrol lubricant showed an opposite trend, and distributed larger droplets. The main effect chart showed a negative, close to linear, trend in droplet size with increased radial distance, similar to that seen in Figure 13. The nonlinear section, also experienced in the work of Park et al. [38], can be explained by the droplet dispersion results. Heavy droplets with high inertia traveling straight out of the nozzle could have obscured the conical path toward zone 6 (50.8 mm, 270°), causing smaller and less droplets in this area. Future testing with the origin set at the center of the collection grid (between zones 5-8) can be conducted for further examination. The effect trendline for channel roughness was nearly horizontal, showing a comparatively weaker relationship between channel roughness and airborne droplet size. This result was further examined by the interaction between lubricant type and channel roughness shown in Figure 17.

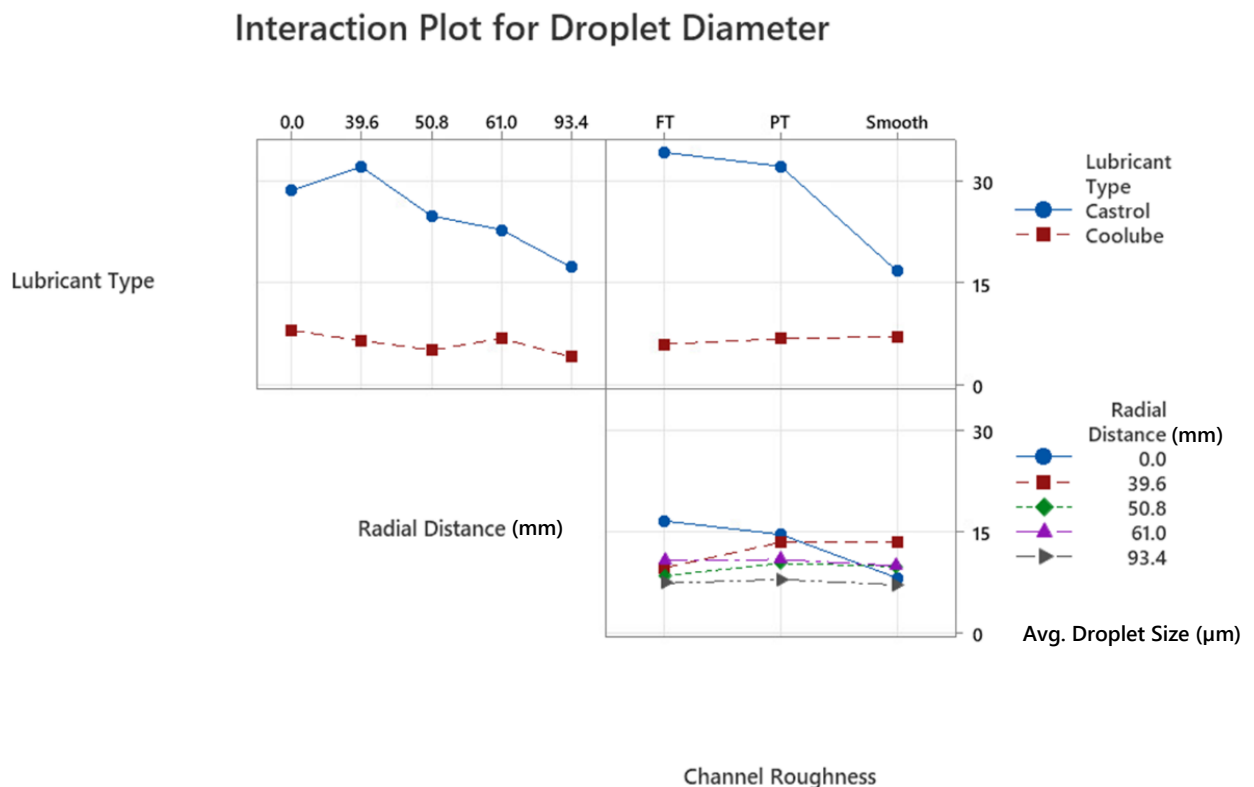


Figure 17. Interaction Between Input Parameters for MQL Droplet Characterization Tests

In the interactions plot, two parameters were said to have minimal interaction when the trendlines in their overlapping region ran parallel to one another. By this notation, there

was little interaction between lubricant type and radial distance, and radial distance and channel roughness. Although only moderate, lubricant type and channel roughness showed the highest level of interaction. This aligned with the results seen in Figure 12, which showed that the lower viscous Coolube lubricant resulted in decreasing airborne droplet size with increased channel roughness, while the opposite trend occurred for the more viscous Castrol lubricant. Flow simulations showed that this was an effect of increased wall adhesion in rougher channels while testing Castrol lubricant, causing less recirculation of small droplets into the downstream airflow. The interaction between lubricant type and channel roughness also explained the small effect of channel roughness on airborne droplet size shown in Figure 16. The opposing trends of Coolube and Castrol lubricants for airborne droplet size with increased channel roughness offset the effect of one another in the smooth and FT channels. This caused the resultant airborne droplet size to show similarly low values for the smooth and FT channels, while the PT channel resulted in a slightly larger size. The interaction between channel roughness and lubricant type would cause the need for designers to account for these factors together at once.

The results of the main effects and interactions plots showed that (i) low viscous lubricant delivered through rough internal channels decreased the airborne droplet size and (ii) airborne droplet size decreased with increased radial distance for low and high viscous lubricants. This agrees with the work of Patil et al. [26] who determined that low viscosity lubricants would form smaller airborne droplets and Khan et al. [3] who showed that increased channel roughness would decrease lubricant droplet diameter.

4.4. Chemical Etching

The surface roughness measurements are shown in Table 12 where T1 and T2 represent trials 1 and 2 respectively.

Table 12. Surface Roughness Before and After Etching. Trials 1 and 2, Each With 4 Random Measurements.

		Before etching	After 5-min etching	Before etching	After 12-min etching	Before etching	After 20-min etching
HA	Average T1, T2 (nm)	N/A	N/A	64, 202	67, 462	62, 125	1001, 997
	Ra S. Deviation T1, T2 (nm)	N/A	N/A	10, 18	9, 11	13, 6	213, 36
HA	Average T1, T2 (nm)	N/A	N/A	97, 292	129, 636	112, 309	1207, 1453
	Sa S. Deviation T1, T2 (nm)	N/A	N/A	6, 51	21, 97	5, 39	49, 139
HA+US	Average T1, T2 (nm)	81, 70	88, 74	72, 56	760, 150	107, 154	1436, 1166
	Ra S. Deviation T1, T2 (nm)	32, 9	31, 7	15, 3	158, 19	6, 3	80, 21
HA+US	Average T1, T2 (nm)	233, 277	263, 293	260, 106	1089, 289	155, 242	1447, 1236
	Sa S. Deviation T1, T2 (nm)	97, 35	108, 37	29, 5	115, 40	31, 19	247, 153

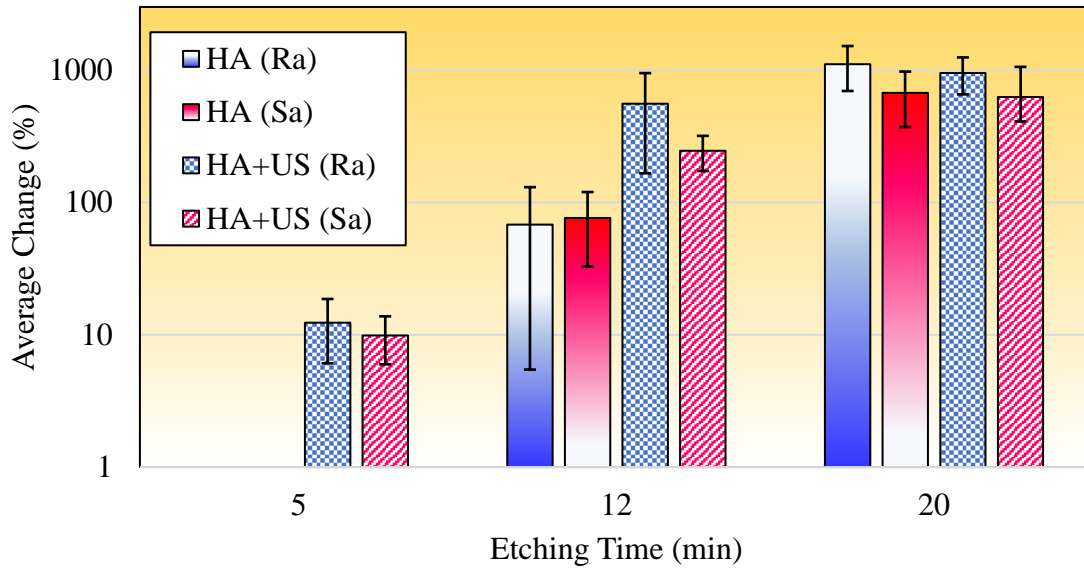


Figure 18. Change in surface roughness of WC-Co with etching time.

Figure 18. shows the percent change in Ra and Sa measurements with time. After 12 minutes of etching the reagent flow caused by ultrasonic pulsation and the occurrence of ultrasonic cavitation caused a greater effect on surface roughness when compared to the exclusively hand manipulated method. At the 20 minute mark the two methods showed similar results in terms of percentage change in Ra and Sa measurements. As the etching time increased, the amount of material that the etching reagent removed reached a maximum, and an upper limit of the resultant surface roughness was formed due to dilution of the etchant with material that had been removed from the tool insert. The following reasons for this variation in experimental results were considered:

1. Some inserts used were significantly rougher to begin the etching trials when compared to other inserts. Rough pre-etched surfaces could have allowed deeper etchant penetration, thus causing more material to be removed. This could have had an effect on the etching process and resultant surface roughness.
2. Hand agitation allowed removal of etching byproduct from the surface of the tool inserts by moving the insert within the reagent bath, thus flushing material from its surface. In this experiment hand agitation was controlled manually. Inconsistencies in the hand agitation could have affected the level of material removal by the etching process, thus causing deviations in the resultant surface roughness.

3. In the experiment a simple hot plate was used to heat the reagent bath. The temperature was measured using a non-contact thermometer throughout each etching run time. Because of this, the operating temperature fell into a range of $60 \pm 10^\circ\text{C}$. This temperature gradient could have affected the etching process.

Figure 19 and Figure 20 show the SEM image results for the 12 minute experiments conducted in trial 1. These images are used to compare the surface roughness between HA and HA + US samples. Figure 19 shows each sample at 1000x magnification. The images in Figure 20 were all captured at 6000x magnification.

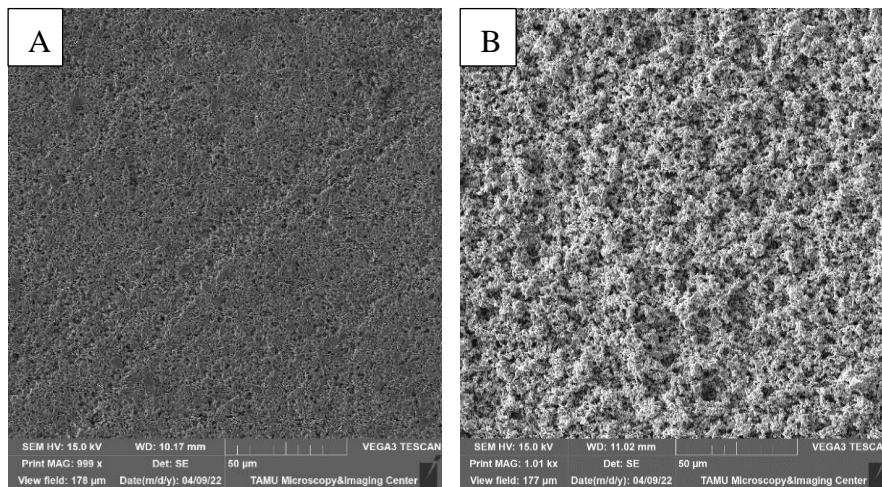


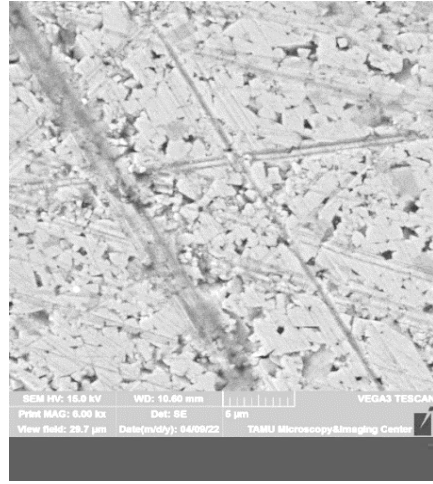
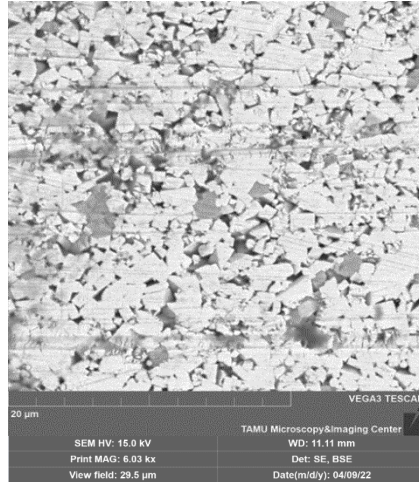
Figure 19. 1000x Image of Etched (A) 12 Minute HA and (B) 12 Minute HA + US Inserts

Figure 19 was captured to show a high level comparison of the surface roughness in each experiment. In the HA sample, the grinding marks from the factory polished surface were still visible. This showed that the 12 minute HA experiment only removed a small layer of material from the insert. In the HA + US sample no grinding marks were visible, and the surface appeared very rough. This showed that the addition of ultrasonic pulsation accelerated the material removal rate in the etching process, resulting in a rougher surface.

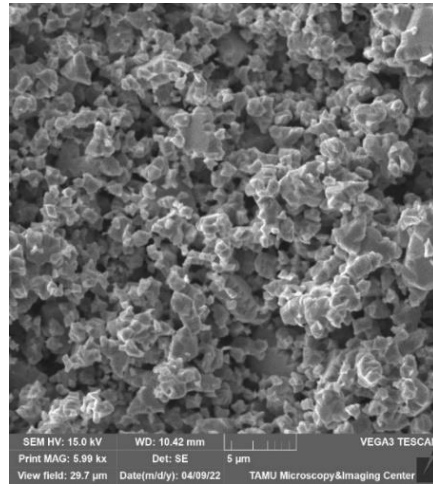
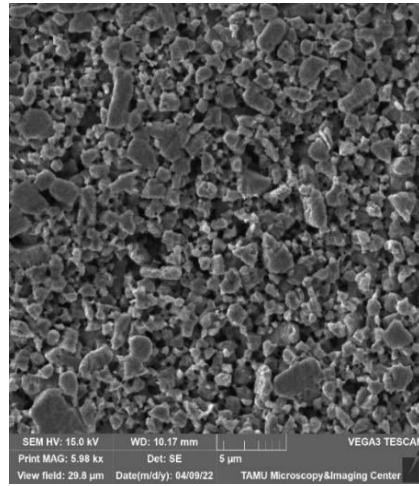
12 Minute HA

12 Minute HA + US

Unetched



Etched



Transition
Area

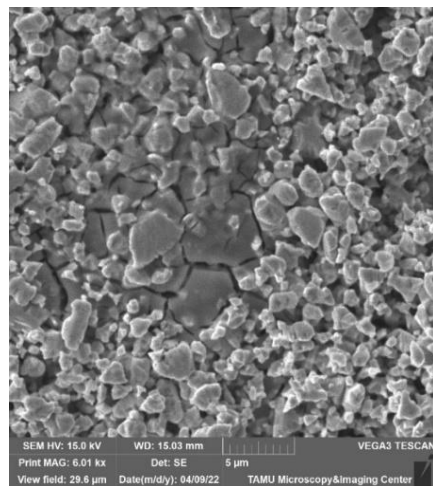
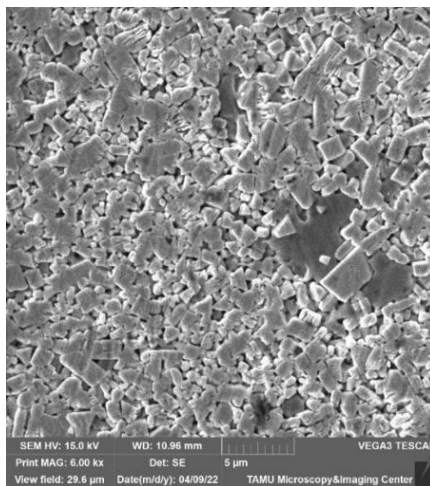


Figure 20. SEM Images for 12 Minute HA and HA + US Trials

Figure 20 showed a comparison of the etched, unetched, and transition regions for the HA and HA + US 12 minute trial 1 experiments. These images were captured at 6000x magnification. The unetched images showed very similar results for the HA and HA + US substrates. In the image captured for the HA tool, a filter was used to differentiate between the WC grains and the Co binder grains. Grinding marks were visible in both images, and the grain sizes were very similar. The etched images showed that the addition of ultrasonic pulsation resulted in a rougher substrate surface. The HA picture showed a much more uniform surface height. More polished carbide grains stayed intact on the surface, causing less area for the etchant to penetrate and remove material. The transition zone of the HA insert showed regions of large and smooth grains that had not been attacked by the etchant. These were surrounded by rougher areas where etching had begun. Comparing the HA and HA + US images drew attention to a negative effect associated with the addition of ultrasonic pulsation. In smooth regions of the HA + US transition zone, crack propagation began on the surface of the insert. After researching the work of Brujan [33], this was concluded to be a result of ultrasonic cavitation. The ultrasonic frequency caused air bubbles to form on the surface of the insert. When those bubbles reached their maximum volumes they burst, sending shock waves crashing into the surface the insert. The shock waves are known to produce pressure in order of 7.7 ± 1.6 GPa [33], which is much larger than the 530 MPa tensile strength of WC-Co. It is believed that this pressure thus caused the surface cracking to occur. These surface cracks are what caused large chunks of material to break off at once, resulting in rougher surfaces.

Figure 21 showed optical images captured on the Olympus STM6 microscope at 50x magnification for the corresponding locations depicted in Figure 17. The scale bar in the lower right corner of each image represents a 50 μ m vertical and horizontal line. The etched image for the 12 minute HA + US specimen was very rough, which caused issues with focus during image capturing. Helicon Focus 8 software was used to stack multiple images in order to create a better focused image.

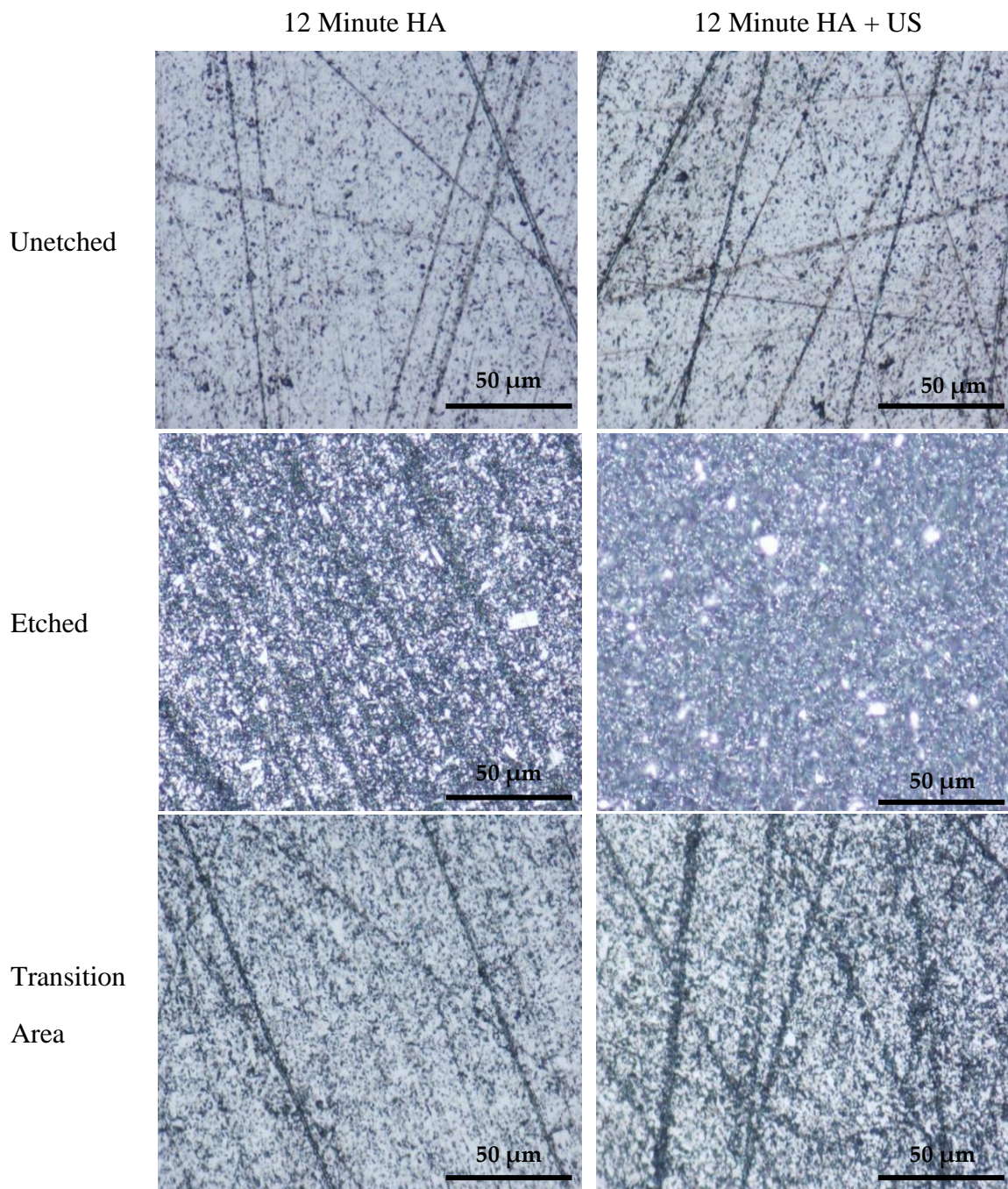


Figure 21. Optical Images for 12 Minute HA and HA + US Trials

The results from the etched and unetched regions support the conclusions drawn from the SEM images. The unetched regions were very similar for the HA and HA + US substrates. Grinding marks were apparent in both, and the images showed that each substrate had similar starting points. For the HA insert, grinding marks were still visible after etching. These grinding marks were fully removed in the HA + US experiment. This supported the conclusion that the addition of ultrasonic pulsation accelerated the material removal rate

during the etching process. The images captured in the transition zones were not as conclusive as the SEM results. The 50x magnification of the optical images was unable to capture the surface cracking seen on the HA + US insert. The grain structures were also unobservable at this magnification level.

Although the external surface of a carbide cutting insert was etched in this study, the material removal mechanism should be the same if etching on the inner surface of coolant channels of carbide tools. By achieving a rough surface of internal channels, MQL using a lubricant with low viscosity can (i) produce finer droplets (ii) generate higher droplet density for uniform lubrication, and (iii) use lubricant efficiently since most lubricant will become airborne droplets rather than adhering to the tool channels. The results of the MQL droplet characterization and chemical etching experiments can be paired to achieve better lubrication properties.

4.5. Sensitivity Analysis

Table 13 shows the sensitivity analysis from this study and the consequences of the known assumptions being incorrect. Two low risk assumptions were made in the MQL droplet characterization portion of the experiment.

1. The main effect of them being false would be a difference in the true airborne droplet volume when compared to those found through calculations. Because oil was slow to evaporate under the tested conditions, and the experimental design was calibrated to decrease coalescence of droplets on the collection grid, these assumptions were presumed to be low risk.
2. The chemical etching of WC-Co experiment resulted in two high risk assumptions. The surface roughness achieved by the etching solution was in order of micrometers, while the roughness tested in the droplet characterization experiment, formed by the threading of the channels, was in order of millimeters. It was presumed that the behavior of aerosol flow would be affected similarly in both scales. Another assumption was made that similar effects would be seen in terms of surface roughening when applying the external etching method to internal lubricant delivery channels. These conclusions were drawn in order to advance the current progress for the problem at hand.

Table 13. Sensitivity Analysis

Assumption	Potential Negative Outcome	Sensitivity
Assuming perfect circles of projected droplets, the projected diameter P was calculated using equation (1)	Estimated droplet volume varies more than calculated. Wetting area becomes slightly inaccurate.	Low Risk Assumption
Assuming no evaporation during flight, no splashing when impacting the glass plate, and no droplet coalescence on the glass plate, an airborne droplet would have the same volume as that on the plate.	Evaporation would cause the amount of lubricant delivered to be less than what was administered. Splashing and coalescence would lead to collected droplets having larger volumes than airborne droplets.	Low Risk Assumption
The effect of increased channel roughness would behave similarly in the micrometer scale as the results formed in the millimeter scale.	This is an approximation to simplify the calculations in order to make progress on the problem being faced. Future work will be used to further address this assumption	High Risk Assumption
The etchant will affect the internal channels similarly to the external surface.	Etching will not make a controllably rough surface in internal channels.	High Risk Assumption

5. CONCLUSIONS*

Selecting a cutting fluid for machining can be a tedious and expensive process of trial and error. Understanding the fundamentals of MQL and physical properties of lubricants allows optimal operation of MQL and achievement of a highly productive environment. Droplet distributions were studied using internal MQL delivered through smooth, partially threaded, and fully threaded tips. This experiment showed:

1. The average droplet diameter decreased as channel roughness increased when testing Coolube lubricant. In Castrol lubricant trials, the opposite effect was shown as the rougher channels created larger droplets due to lubricant coalescence and channel wall adhesion.
2. For both lubricant types, the average droplet size and count decreased as a function of increased radial distance. This showed that the dispersion of lubricant was most concentrated directly beneath the outlet tip, and decreased at further collection points.
3. Coolube lubricant performed more consistently than Castrol and better represented the hypothesized relationship. The research team believed that the higher viscosity of Castrol lubricant led to lubrication coalescence at the outlet of the tip, a phenomenon that was exacerbated by the rougher channels. This caused large droplets to break off and land on the collection grid, skewing the droplet distributions.

Chemical etching processes were used to characterize the effect of a 90% H₂O₂ 10% HNO₃ etchant on the surface roughness of WC-Co (6% Co) tool inserts as a function of time. The following conclusions were drawn from this experiment:

1. The addition of ultrasonic pulsation accelerated the material removal rate and surface roughening in the 12 minute trials. At the 20 minute point similar results were seen for the change in surface roughness between experiments that did and did not incorporate ultrasonic pulsation. This suggested that there was an upper limit to the surface roughness achievable before refreshing the etchant.

*Reprinted with permission from “Effect of Channel Roughness on Micro-Droplet Distribution in Internal Minimum Quantity Lubrication” Craig M., Raval J., Tai B., Patterson A., and Hung W., Dynamics, vol. 2, no. 4, pp. 336–355, by the authors 2022.

2. Outlying points on the change in roughness versus time plots were thought to be caused by differences in the production batches of the tool inserts, irregularities in the amount of hand agitation during each experiment, and instability of the operating temperature during each run.

3. Optical images showed that the tool inserts started with similar surface structures. The HA + US experiments led to rougher surfaces in etched regions when compared to the HA runs. In transition zones between etched and unetched areas, surface cracking was visible on the HA + US substrates. This was believed to be caused by the bursting of ultrasonic cavitation air bubbles.

6. FUTURE WORK

The continuation of these research efforts can be broken down into the following future tasks:

1. Etching experiments will be tested on the internal lubricant delivery channels of MQL drills. It is recommended that etchant be pumped through the channels while the drill is ultrasonically vibrated directly or via an ultrasonic bath.
2. Lubricant flow simulations will be conducted by incorporating the resultant surface roughness created in the etching trials from this experiment.
3. Further trials will be conducted to verify the results of the microdroplet distributions by incorporating the channel roughness created in the etching trials from this experiment. It is recommended that multiple low and high viscous lubricants are tested and statistical analysis is completed to compare the effect of channel roughness on airborne droplet size.
4. The effect of resultant droplets, induced by internal channel surface roughness, will be quantified by drilling operations.

REFERENCES

- [1] Sharma V. S., Singh G. R., and Sorby G. R. “A review on minimum quantity lubrication for machining processes,” *Materials and Manufacturing Processes*, vol. 30, no. 8, pp. 935–953, 2014.
- [2] Tai B., Stephenson D. A., Furness R. J., and Shih A. J. “Minimum quantity lubrication (MQL) in Automotive Powertrain Machining,” *Procedia CIRP*, vol. 14, pp. 523–528, 2014.
- [3] Khan W. A. “Through-Tool Minimum Quantity Lubrication and Effect on Machinability.” *Journal of Manufacturing Processes*, vol. 34, 2018, pp. 750–757.,
<https://doi.org/10.1016/j.jmapro.2018.03.047>.
- [4] Stephenson D. A., and Agapiou J. S., in *Metal cutting theory and practice*, Boca Raton: CRC Press, 2019, pp. 803–822.
- [5] Race A., Zwierzak I., Secker J., Walsh J., Carrell J., Slatter T., and Maurotto A., “Environmentally sustainable cooling strategies in milling of SA516: Effects on surface integrity of dry, flood and MQL machining,” *Journal of Cleaner Production*, vol. 288, p. 125580, 2021.
- [6] Hwang Y. K., and Lee C. M., “Surface roughness and cutting force prediction in MQL and wet turning process of AISI 1045 using design of Experiments,” *Journal of Mechanical Science and Technology*, vol. 24, no. 8, pp. 1669–1677, 2010.
- [7] Li K.M., and Lin C.P., “Study on minimum quantity lubrication in micro-grinding,” *The International Journal of Advanced Manufacturing Technology*, vol. 62, no. 1-4, pp. 99–105, 2011.
- [8] Tasdelen B., Wikblom T., and Ekered S., “Studies on minimum quantity lubrication (MQL) and air cooling at drilling,” *Journal of Materials Processing Technology*, vol. 200, no. 1-3, pp. 339–346, 2008.
- [9] Maruda R. W., Feldshtein E., Legutko S., and Krolczyk G. M., “Research on Emulsion Mist Generation in the Conditions of Minimum Quantity Cooling Lubrication (MQCL),” *Tehnički vjesnik*, vol. 22, no. 5, 2015.

- [10] Maruda R. W., Krolczyk G. M., Feldshtein E., Pusavec F., Szydłowski M., Legutko S., Sobczak-Kupiec A., “A study on droplets sizes, their distribution and heat exchange for minimum quantity cooling lubrication (MQCL),” *International Journal of Machine Tools and Manufacture*, vol. 100, pp. 81–92, 2016.
- [11] Raval J. K., and Tai B. “An optical tomographic method to characterize the mist distribution in MQL Tools,” *Journal of Manufacturing Processes*, vol. 62, pp. 275–282, 2021.
- [12] Raval J. K., Kao Y. T., and Tai B. “Characterizing mist distribution in through-tool minimum quantity lubrication drills,” *Journal of Manufacturing Science and Engineering*, vol. 142, no. 3, 2020.
- [13] Kao Y. T., Takabi B., Hu M., and Tai B. “Coolant Channel and flow characteristics of MQL drill bits: Experimental and numerical analyses,” *Volume 2: Additive Manufacturing; Materials*, 2017.
- [14] Yıldırım Ç. V., Kıvak ., Sarıkaya M., and Erzincanlı F. “Determination of MQL parameters contributing to sustainable machining in the milling of nickel-base superalloy Waspaloy,” *Arabian Journal for Science and Engineering*, vol. 42, no. 11, pp. 4667–4681, 2017.
- [15] Tai B., Dasch J. M., and Shih A. J. “Evaluation and comparison of lubricant properties in minimum quantity lubrication machining,” *Machining Science and Technology*, vol. 15, no. 4, pp. 376–391, 2011.
- [16] Chinchankar S., and S. K. Choudhury, “Hard turning using HiPIMS-coated carbide tools: Wear behavior under dry and minimum quantity lubrication (MQL),” *Measurement*, vol. 55, pp. 536–548, 2014.
- [17] Said Z., Gupta M., Hegab H., Arora N., Khan A. M., Jamil M., and Bellos E. “A comprehensive review on minimum quantity lubrication (MQL) in machining processes using nano-cutting fluids,” *The International Journal of Advanced Manufacturing Technology*, vol. 105, no. 5-6, pp. 2057–2086, 2019.

- [18] Carou D., Rubio E., and Davim J. P. “A note on the use of the minimum quantity lubrication (MQL) system in turning,” *Industrial Lubrication and Tribology*, vol. 67, no. 3, pp. 256–261, 2015.
- [19] Davim J. P., Sreejith P. S., and Silva J., “Turning of brasses using minimum quantity of lubricant (MQL) and flooded lubricant conditions,” *Materials and Manufacturing Processes*, vol. 22, no. 1, pp. 45–50, 2007.
- [20] Dhar N. R., Kamruzzaman M., and Ahmed M. “Effect of minimum quantity lubrication (MQL) on tool wear and surface roughness in turning Aisi-4340 Steel,” *Journal of Materials Processing Technology*, vol. 172, no. 2, pp. 299–304, 2006.
- [21] Chetan, Behera B. C., Ghosh S., Rao P. V., “Wear behavior of PVD tin coated carbide inserts during machining of Nimonic 90 and ti6al4v superalloys under dry and MQL conditions,” *Ceramics International*, vol. 42, no. 13, pp. 14873–14885, 2016.
- [22] Kishawy H. A., Dumitrescu M., Ng E. G., and Elbestawi M. A. “Effect of coolant strategy on tool performance, Chip Mor-phology and surface quality during high-speed machining of A356 aluminum alloy,” *International Journal of Machine Tools and Manufacture*, vol. 45, no. 2, pp. 219–227, 2005.
- [23] Iskandar Y., Tendolkar A., Attia M. H., Hendrick P., Damir A., and Diakodimitris C., “Flow visualization and characterization for optimized MQL machining of Composites,” *CIRP Annals*, vol. 63, no. 1, pp. 77–80, 2014.
- [24] Rahim E. A., and Sasahara H. “Investigation of tool wear and surface integrity on MQL machining of ti-6al-4v using biode-gradable oil,” *Proceedings of the Institution of Mechanical Engineers, Part B: Journal of Engineering Manufacture*, vol. 225, no. 9, pp. 1505–1511, 2011.
- [25] Davim J.P., Sreejith P.S., Gomes R., and Peixoto C., “Experimental studies on drilling of aluminium (AA1050) under dry, minimum quantity of lubricant, and flood-lubricated conditions,” *Proceedings of the Institution of Mechanical Engineers, Part B: Journal of Engineering Manufacture*, vol. 220, no. 10, pp. 1605–1611, 2006.

- [26] Patil A., Javal J., Bangma T., Edinbarough I., Obeidat S., Stephenson D., Tai B., and Hung N.P., "Characterization and Performance of Minimum Quantity Lubricants in Through-Tool Drilling," *Journal of Engineering Materials and Manufacture*, 5(4), August 2020, pp. 98-115. DOI: <https://doi.org/10.26776/ijemm.05.04.2020.01>
- [27] Sadeghi M. H., Haddad M. J., Tawakoli T., and Emami M., "Minimal quantity lubrication-MQL in grinding of ti-6al-4v titanium alloy," *The International Journal of Advanced Manufacturing Technology*, vol. 44, no. 5-6, pp. 487-500, 2008.
- [28] Sadeghi M. H., Hadad M. J., Tawakoli T., Vesali A., and Emami M., "An investigation on surface grinding of AISI 4140 hardened steel using minimum quantity lubrication-MQL technique," *International Journal of Material Forming*, vol. 3, no. 4, pp. 241-251, 2010.
- [29] Haubner R., Kubelka, Lux S., Griesser B., Grasserbauer, M. (1995). Murakami and H₂SO₄/H₂O₂ Pretreatment of WC-Co Hard Metal Substrates to Increase the Adhesion of CVD Diamond Coatings. *Le Journal De Physique IV*, 05(C5).
<https://doi.org/10.1051/jphyscol:1995589>
- [30] Chakravarthy, Chandran M., Bhattacharya S. S., Rao M. S. R., and Kamaraj M. (2012). A comparative study on wear behavior of tin and diamond coated WC-co substrates against hypereutectic al-Si Alloys. *Applied Surface Science*, 261, 520-527.
<https://doi.org/10.1016/j.apsusc.2012.08.049>
- [31] Sha L., Zhiming Y., Danqing Y., and Yongxia L. (2001). Chemical pretreatments at the surface of WC-15 wt% co for diamond coatings. In Wildner, H. (Ed.). *Powder metallurgical high performance materials Proceedings Volume 2: P/M hard materials*, (p. 896). Austria
- [32] Jung S.-W., Kim J., and Kang S.-J. L. (2001). Etching for microstructural observation of cemented submicrometer-sized carbides. *Journal of the American Ceramic Society*, 84(4), 899-901. <https://doi.org/10.1111/j.1151-2916.2001.tb00765.x>
- [33] Brujan E. A., Ikeda T., and Matsumoto Y. (2008). On the pressure of cavitation bubbles. *Experimental Thermal and Fluid Science*, 32(5), 1188-1191.
<https://doi.org/10.1016/j.expthermflusci.2008.01.006>

- [34] Pecha R., and Gompf B. (2000). Microimplosions: Cavitation collapse and shock wave emission on a nanosecond time scale. *Physical Review Letters*, 84(6), 1328–1330.
<https://doi.org/10.1103/physrevlett.84.1328>
- [35] AZO Materials. (2022, March 22). Properties: Tungsten carbide - an overview. AZoM.com. Retrieved April 10, 2022, <https://www.azom.com/properties.aspx?ArticleID=1203>
- [36] Tungsten Carbide Grade Chart. Federal Carbide. Retrieved April 10, 2022, https://www.federalcarbide.com/tungsten_carbide_grade_chart.html
- [37] Gibbs J. W., *The scientific papers in two volumes*. New York: Dover, 1961.
- [38] Park K.H., Olortegui-Yume J.A., Joshi S., Kwon P., Yoon M.C., Lee G.B., and Park S.B., “Measurement of droplet size and distribution for minimum quantity lubrication (MQL),” 2008 International Conference on Smart Manufacturing Application, 2008.

APPENDIX A. MQL DROPLET CHARACTERIZATION DATA

Table A1. Lubricant CL Airborne Droplet Data for Smooth Channel

Location	Radial Distance From Origin (mm)	Avg Airborne Drop- let Diameter (μm)	Stdev (μm)	Count
1	61	5.22	4.25	465
2	93.4	4.38	3.98	384
3	61	6.04	4.52	714
4	93.4	4.31	3.89	369
5	0	9.67	8.39	1832
6	50.8	5.81	3.92	611
7	39.6	7.12	6.03	938
8	39.6	6.54	5.15	821

Table A2. Lubricant CL Airborne Droplet Data for FT Channel

Location	Radial Distance From Origin (mm)	Avg Airborne Drop- let Diameter (μm)	Stdev (μm)	Count
1	61	4.50	2.28	774
2	93.4	3.75	2.85	316
3	61	5.37	4.40	599
4	93.4	3.58	2.83	306
5	0	7.78	6.32	2314
6	50.8	4.88	3.80	654
7	39.6	10.13	8.11	1288
8	39.6	5.31	4.91	742

Table A3. Lubricant CL Airborne Droplet Data for PT Channel

Location	Radial Distance From Origin (mm)	Avg Airborne Drop- let Diameter (μm)	Stdev (μm)	Count
1	61	4.50	2.28	774
2	93.4	3.75	2.85	316
3	61	5.37	4.40	599
4	93.4	3.58	2.83	306
5	0	7.78	6.32	2314
6	50.8	4.88	3.80	654
7	39.6	10.13	8.11	1288
8	39.6	5.31	4.91	742

Table A4. Lubricant CT Airborne Droplet Data for Smooth Channel

Location	Radial Distance From Origin (mm)	Avg Airborne Droplet Diameter (μm)	Stdev (μm)	Count
1	61	7.02	7.88	474
2	93.4	5.73	7.39	159
3	61	8.09	6.87	184
4	93.4	4.54	6.31	290
5	0	16.71	15.24	624
6	50.8	7.38	8.27	304
7	39.6	11.49	13.34	394
8	39.6	14.44	13.82	318

Table A5. Lubricant CT Airborne Droplet Data for FT Channel

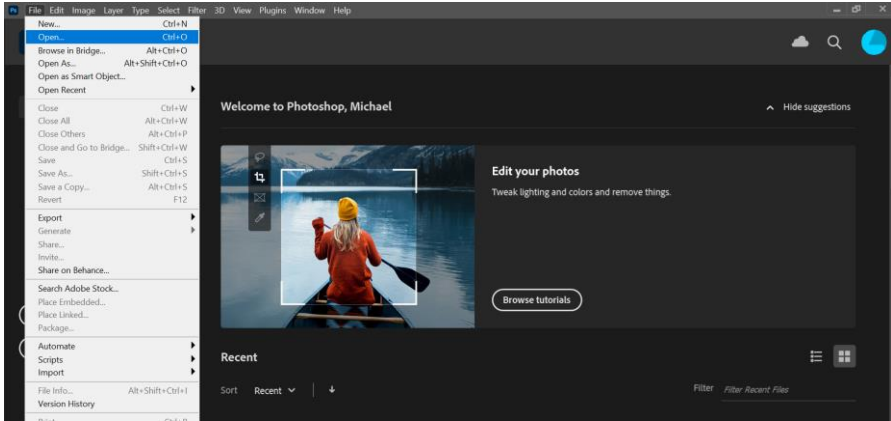
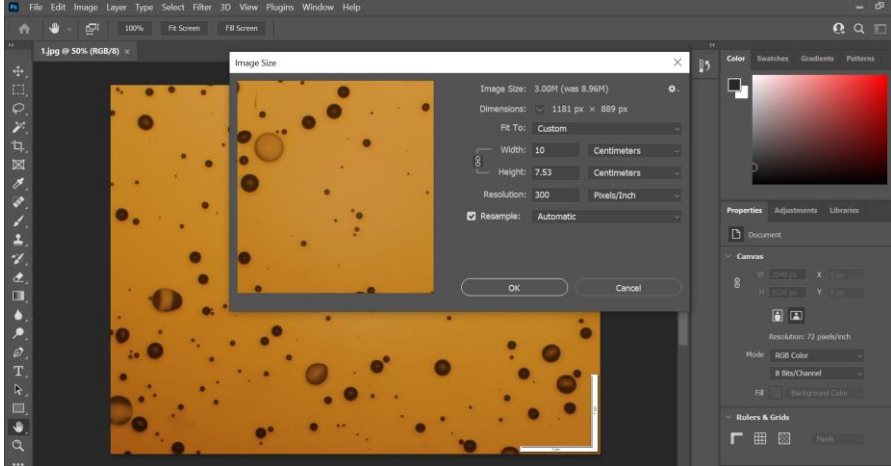
Location	Radial Distance From Origin (mm)	Avg Airborne Droplet Diameter (μm)	Stdev (μm)	Count
1	61	16.27	10.66	225
2	93.4	11.71	8.89	105
3	61	11.21	8.54	187
4	93.4	9.58	7.09	77
5	0	16.72	12.41	655
6	50.8	14.70	9.07	168
7	39.6	15.82	10.84	272
8	39.6	14.83	10.16	360

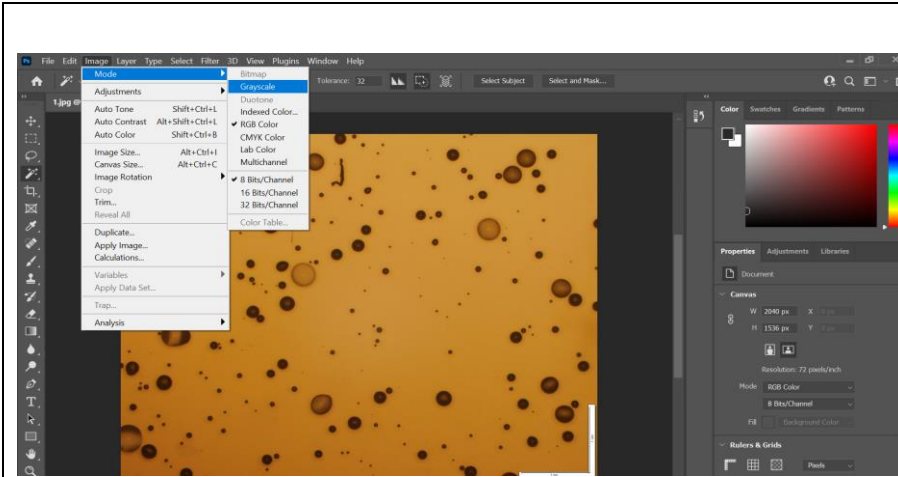
Table A6. Lubricant CT Airborne Droplet Data for PT Channel

Location	Radial Distance From Origin (mm)	Avg Airborne Droplet Diameter (μm)	Stdev (μm)	Count
1	61	12.37	9.04	308
2	93.4	9.28	7.51	104
3	61	9.93	8.37	197
4	93.4	9.27	7.13	83
5	0	19.73	17.68	549
6	50.8	12.59	12.09	212
7	39.6	13.66	11.88	309
8	39.6	13.03	12.54	283

APPENDIX B. MICROSCOPE IMAGE PROCESSING

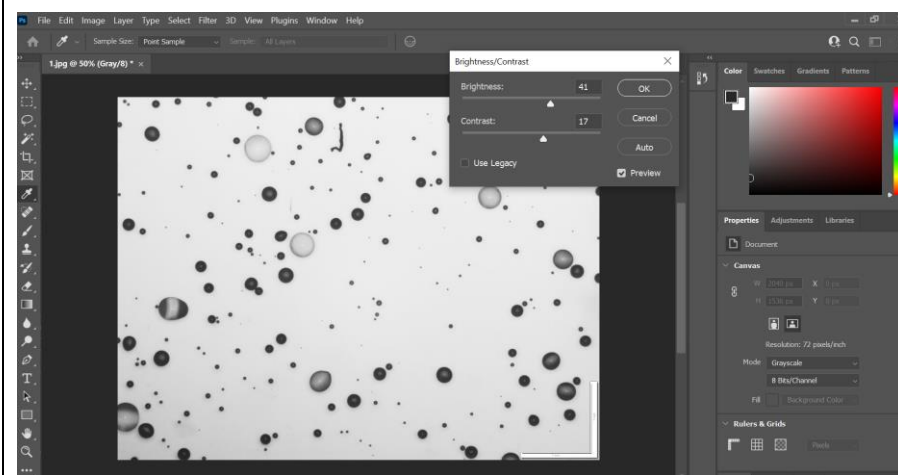
Image processing was completed using Adobe Photoshop v 22.5.1 to create grayscale images and ImageJ 1.52a to capture the projected droplet diameters. Tables B1 and B2 detail the steps necessary to edit images in Adobe Photoshop and ImageJ respectively. These processes were modified from the procedure used by Patil [26].

<h3>Table B1. Adobe Photoshop Image Processing</h3>	
 <p>The screenshot shows the Adobe Photoshop interface. The 'File' menu is open, and the 'Open' option is highlighted. The main workspace displays a welcome message and a preview of a photo of a person in a kayak on a lake. The 'Recent' panel is visible at the bottom.</p>	<ol style="list-style-type: none"> 1. Open Adobe Photoshop and upload the microscope picture to be edited. File → Open
 <p>The screenshot shows the Adobe Photoshop interface with the 'Image Size' dialog box open. The dialog box displays the following settings: Image Size: 3.00M (was 8.96M), Dimensions: 1181 px x 889 px, Resolution: 300 Pixels/Inch, and Resample: Automatic. The background shows a microscopic image of droplets on a brown surface.</p>	<ol style="list-style-type: none"> 2. Adjust the image size to 10 cm in width and 300 pixels/inch. Image → Image Size <p>Note: The height dimension will automatically adjust.</p>

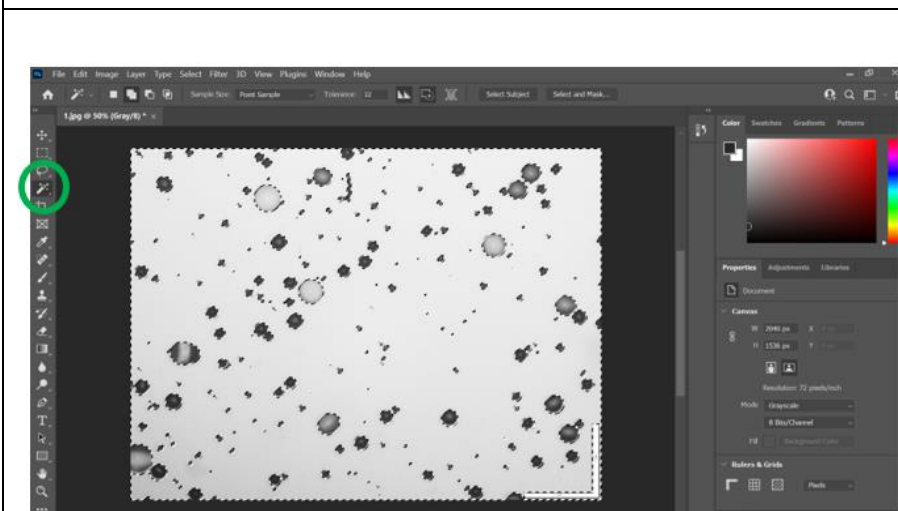


3. Convert the image to grayscale.
Image → Mode → Grayscale

Note: If a message box displays asking to discard color information, select discard

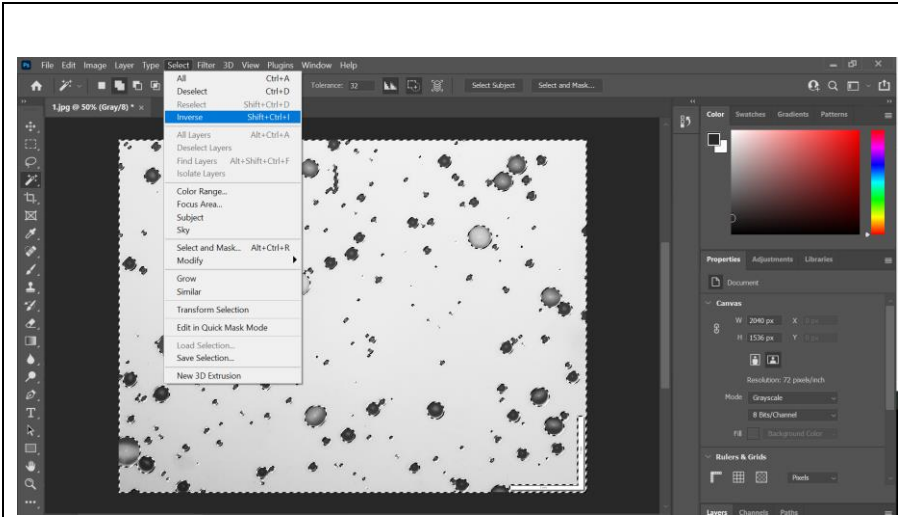


4. Adjust the brightness and contrast to draw a sharper boundary between the droplets and background.
Image → Adjustments → Brightness and Contrast

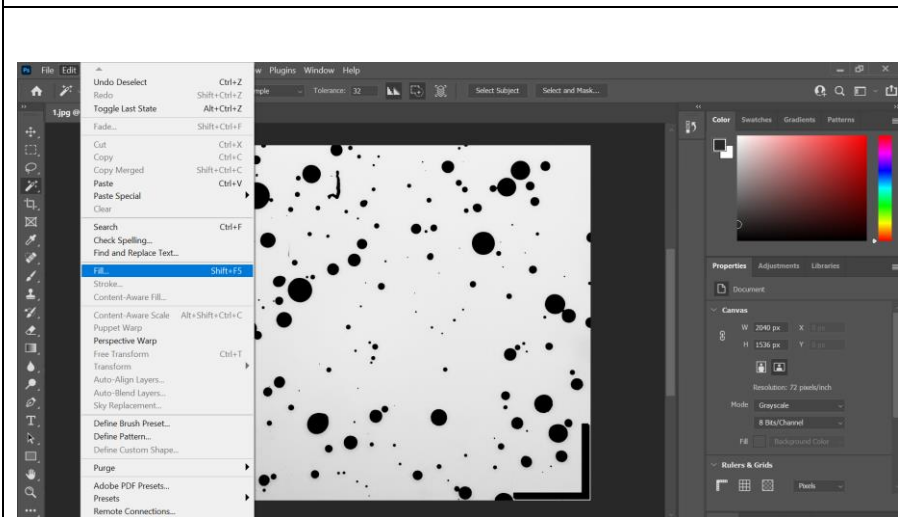


5. Using the Magic Wand tool, select the background area surrounding the droplets.

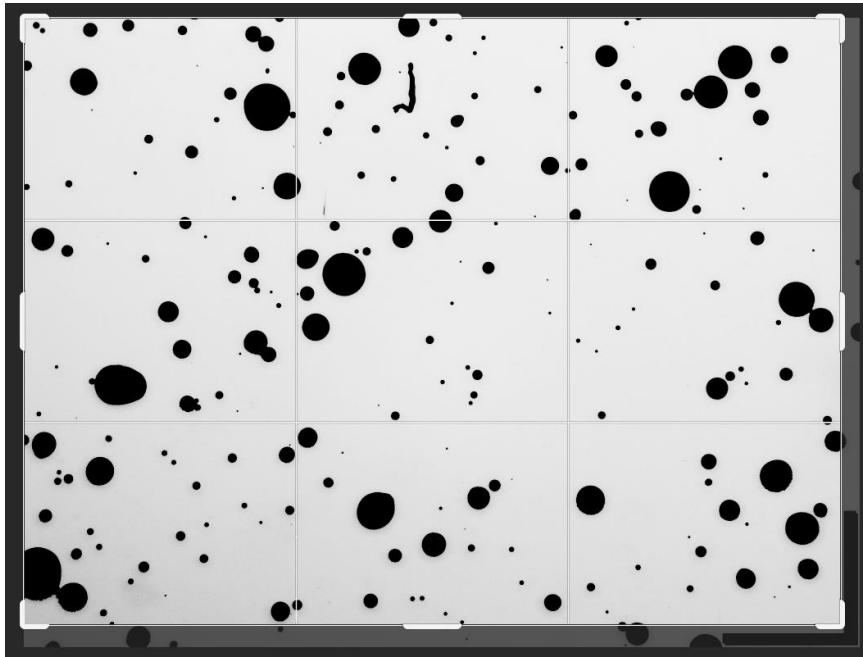
Note: The Magic Wand tool is located on the tool bar on the left side of the screen.



6. Inverse the selection such that the droplets are selected. Select → Inverse

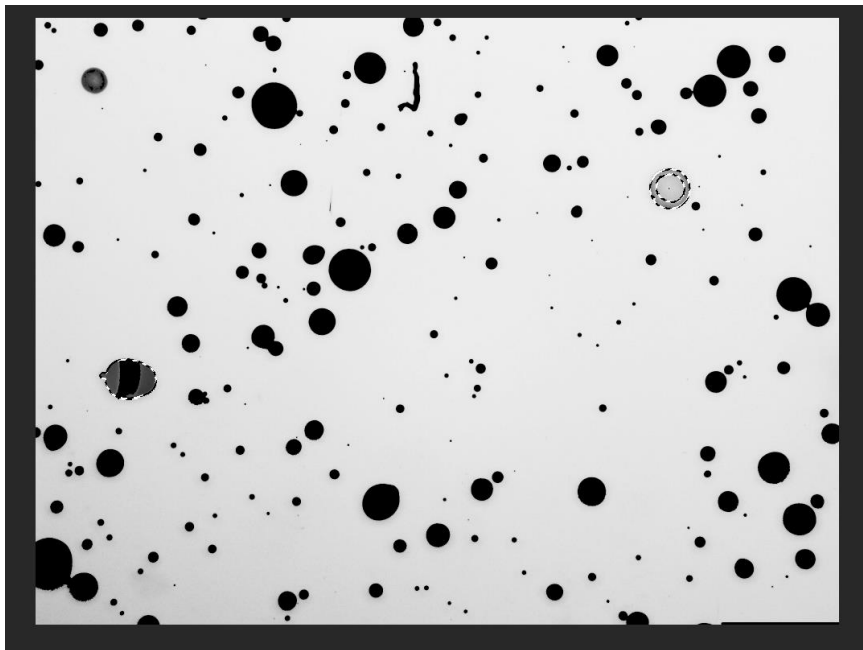


7. Fill the droplets in black. Edit → Fill → Black

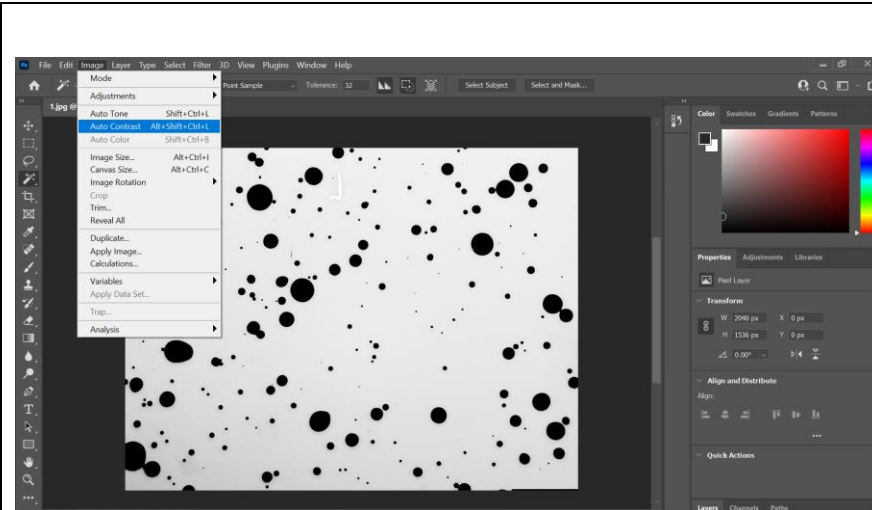


8. Crop the image to eliminate the scale bar in the bottom right corner.

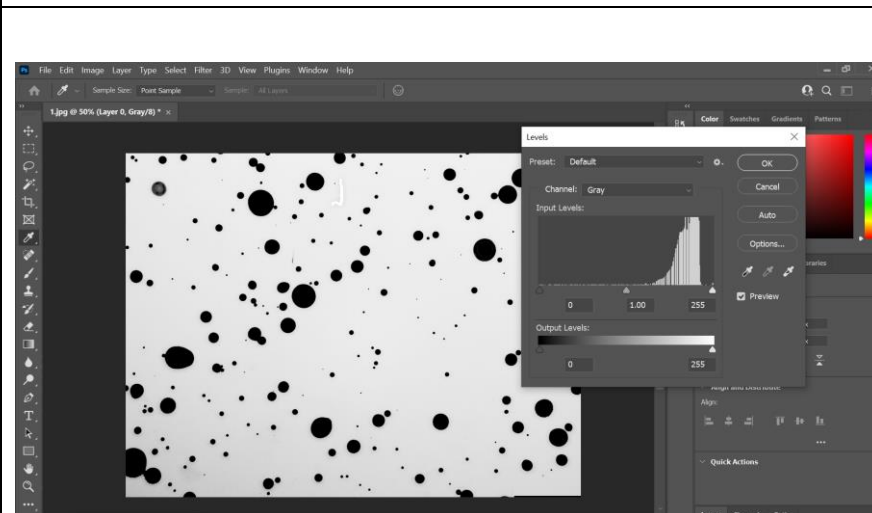
Note: The Crop tool is located on the tool bar on the left side of the screen.



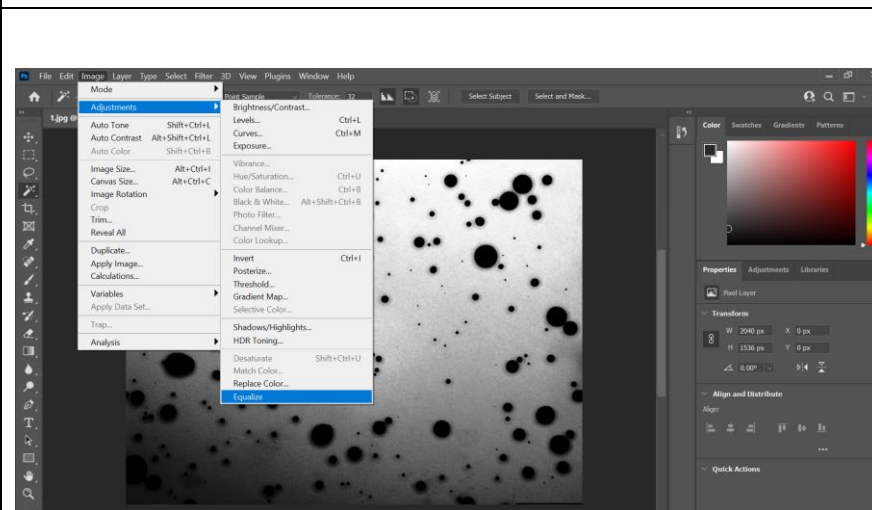
9. If any droplets were not selected nor filled black, the magic wand tool can be used to select them individually. Once selected repeat step 6. Repeat until all droplets are filled black.



10. Auto-adjust the brightness and contrast settings. Image → Auto Contrast

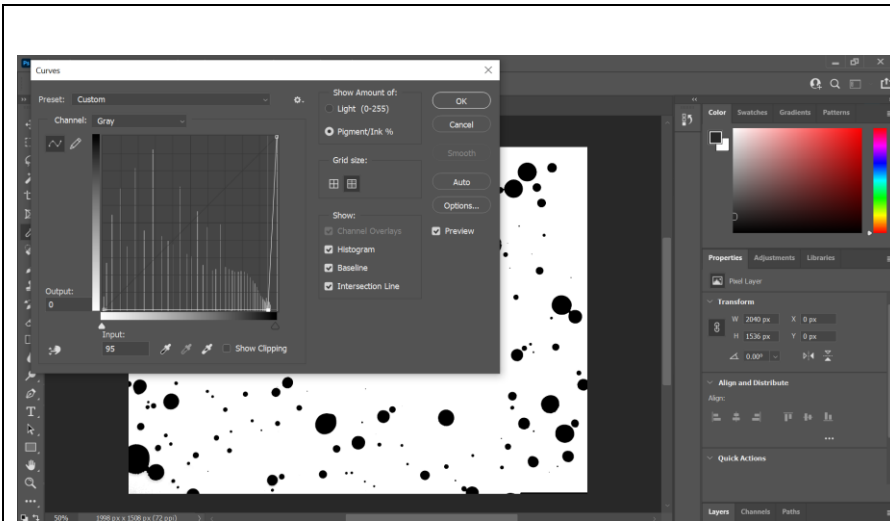


11. Auto-adjust the image levels to correct the image tonal adjustments. Image → Adjustments → Levels → Auto



12. Equalize the image to turn light areas white and dark areas black. Image → Adjustments → Equalize

Note: Repeat step 9 if necessary

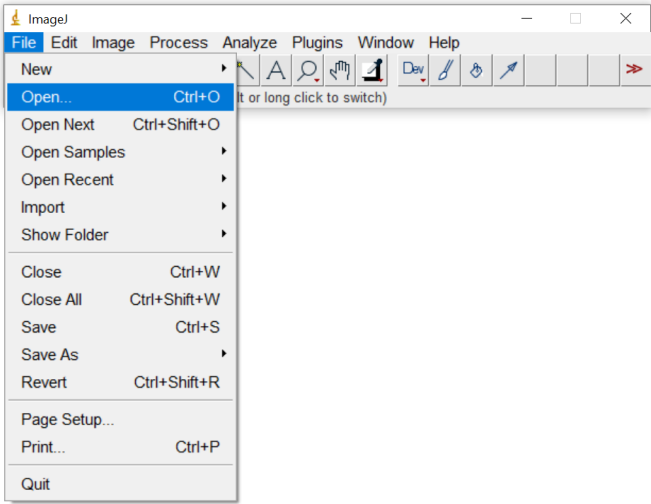
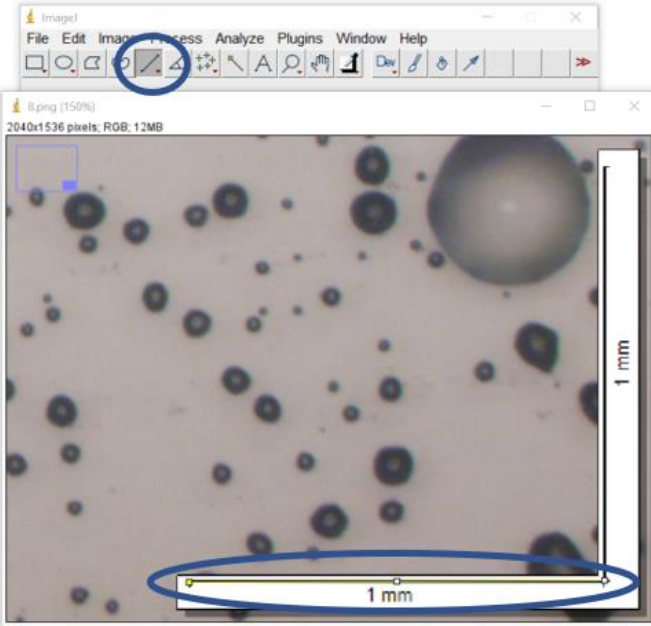


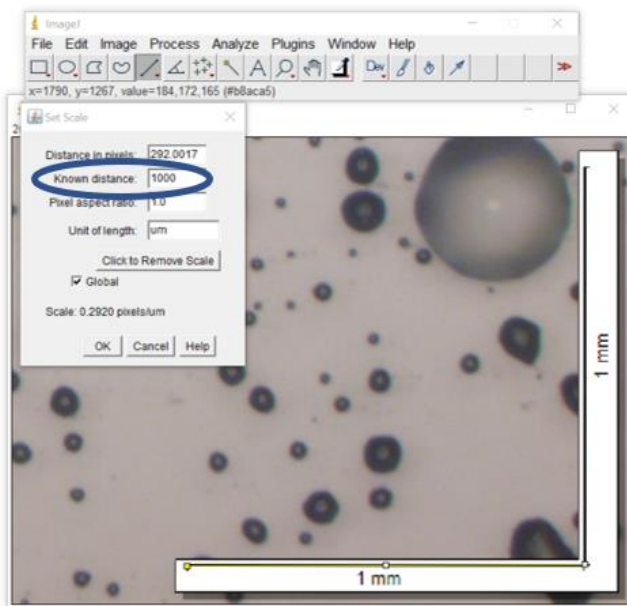
13. Perform tonal adjustments using the curves setting. Image → Adjustments → Curves

Note: Click and drag the curve until a crisp black and white image is obtained. Record the input and output values for batch processing

14. Save the image. File → Save As

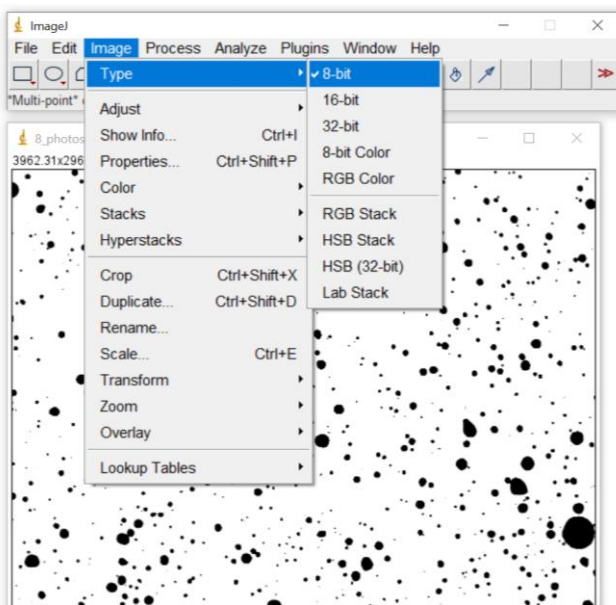
Table B2. ImageJ Image Processing

 <p>The screenshot shows the ImageJ application window with the 'File' menu open. The 'Open...' option is highlighted in blue, and its keyboard shortcut 'Ctrl+O' is visible. Other menu items include 'New', 'Open Next', 'Open Samples', 'Open Recent', 'Import', 'Show Folder', 'Close', 'Close All', 'Save', 'Save As', 'Revert', 'Page Setup...', 'Print...', and 'Quit'. The toolbar is partially visible at the top right of the menu.</p>	<p>1. Open the original microscope image corresponding to the Adobe Photoshop edited image. File → Open</p>
 <p>The screenshot shows the ImageJ interface with a microscope image open. The 'Line' tool in the toolbar is circled in blue. The image contains a scale bar at the bottom right labeled '1 mm'. A yellow line is drawn along the bottom edge of the image, also labeled '1 mm'. The image title bar indicates '8.png (150%)' and '2040x1536 pixels, RGB, 12MB'.</p>	<p>2. Use the line tool to draw a line along the 1 mm scale in the bottom right corner of the image.</p>

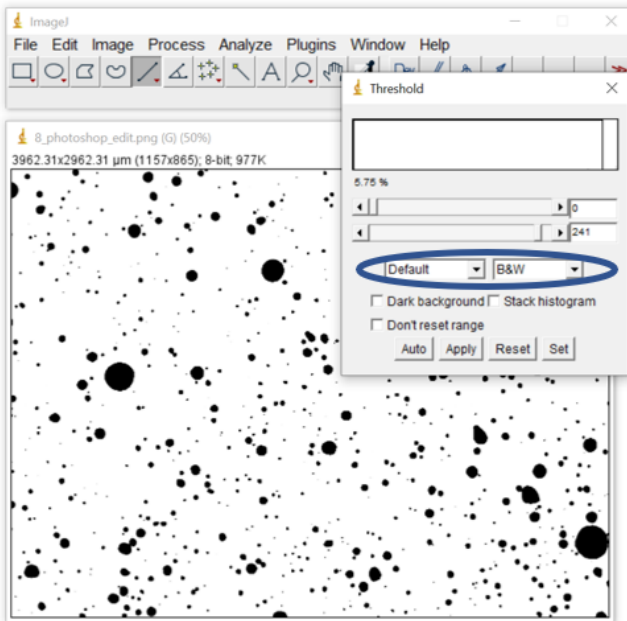


3. Set the scale. ImageJ calculates the length of the line generated in step 2 and records it in the Distance in pixels box under the set scale window. Analyze → Set Scale → Known Distance: 1000 → Unit of length: μm → Check the Global selection box to hold this scale for batch editing

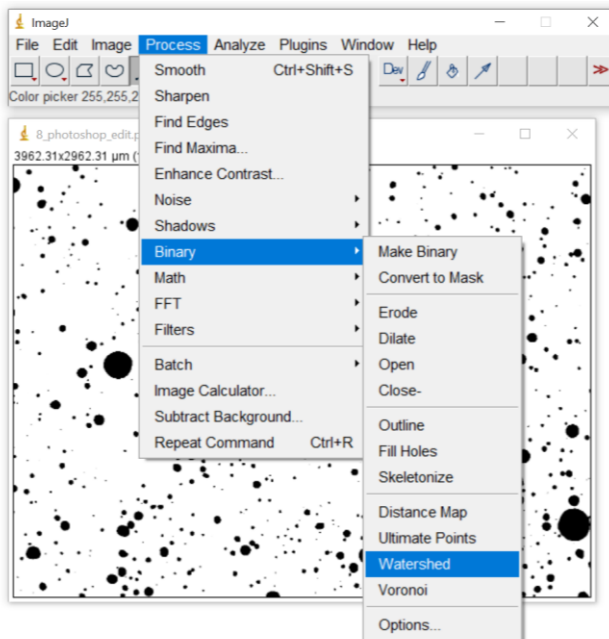
Note: Known distance is set to 1000 because the Unit of length is set to μm and the microscope image scale was $1\text{mm} = 1000 \mu\text{m}$



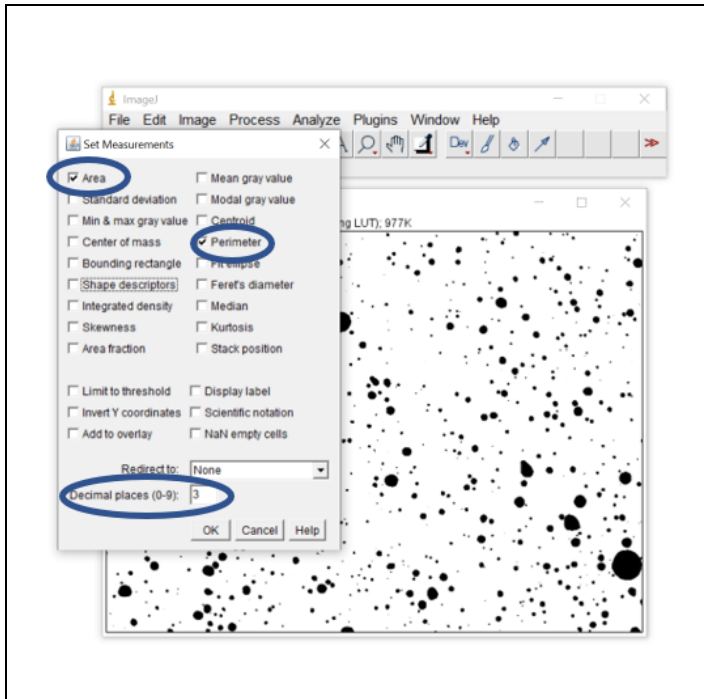
4. Using the procedure from step 1 open the Adobe Photoshop edited picture. Convert to 8-bit. Image → Type → 8 Bit



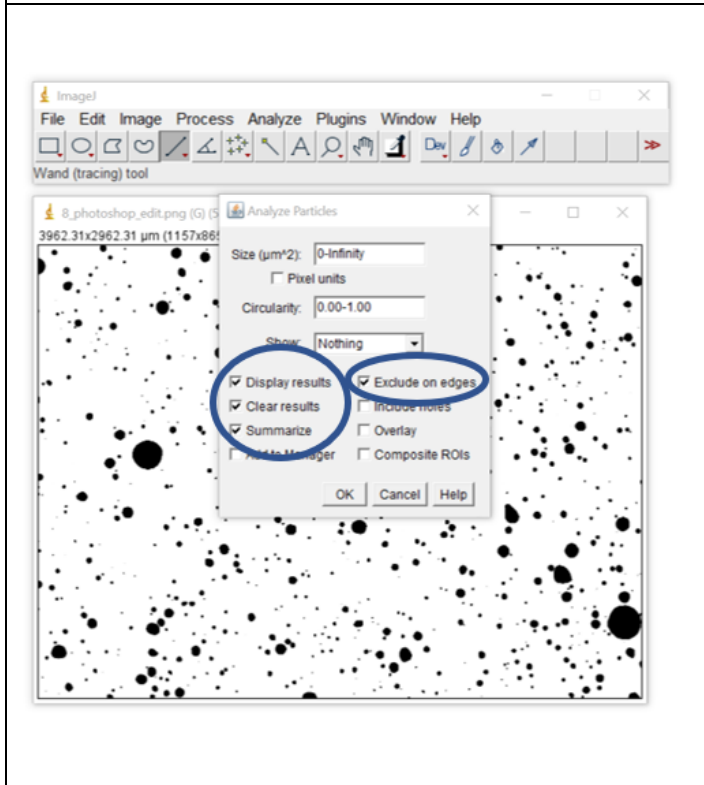
5. Adjust the threshold such that the droplets are uniformly filled and have sharp contrast with the background. Image → Adjust → Threshold → Select Default and B&W → Adjust the Scales as necessary → Apply



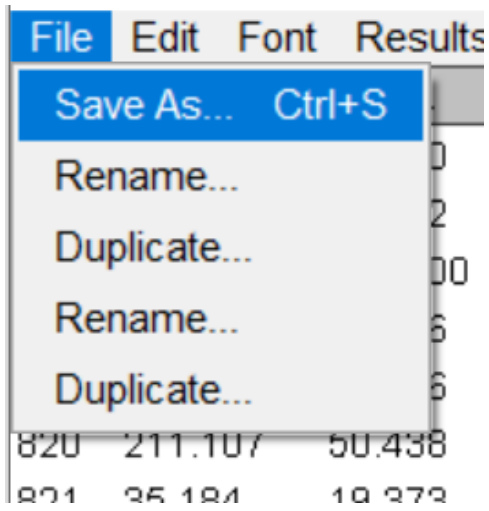
6. Separate any merged droplets using the watershed function. Process → Binary → Watershed



7. Select the necessary measurements for the final results. This experiment collected measurements for area and perimeter using a decimal place limit of 3. Analyze → Set Measurements → Check the area and perimeter selection boxes → Decimal places: 3



8. Calculate the projected droplet areas. Analyze → Analyze Particles → Check the Display results, Clear results, Summarize, and Exclude on edges selection boxes



9. Using the File → Save As function on each tab, save the results, summary, and images generated.

APPENDIX C. CHEMICAL ETCHING DATA

Tables C1-C20 show the raw data collected for the Ra and Sa measurements for each tool insert. In these tables K represents the grinded (polished) side of the insert while B represents the bottom. E and C are used to describe the edge and center locations of each measurement. For example KE means polished side edge.

Table C1. Trial 1 12 min HA Ra Measurements (nm)

		KE	KC	BE	BC
Pre-Etching	M1	75.22	46.10	48.70	47.53
	M2	76.45	52.70	57.60	46.91
	M3	77.30	55.19	63.82	51.63
	M4	77.56	64.34	67.11	53.01
	M5	79.44	80.53	87.38	63.00
	Avg	77.19	59.77	64.92	52.42
Post-Etching	M1	76.44	80.48	59.31	63.90
	M2	77.58	43.70	42.00	40.50
	M3	78.13	60.08	64.91	47.40
	M4	80.49	61.90	67.43	61.27
	M5	83.51	66.02	110.58	71.71
	Avg	79.23	62.44	68.84	56.96
Average Percent Change		2.64	2.64	4.46	6.04
Average Delta Ra (nm)		2.04	2.04	2.67	3.92

Table C2. Trial 1 20 min HA Ra Measurements (nm)

		KE	KC	BE	BC
Pre-Etching	M1	61.70	55.10	45.30	50.25
	M2	78.93	63.10	45.46	57.71
	M3	85.77	67.36	52.56	44.99
	M4	93.71	69.71	58.03	48.25
	M5	74.70	70.20	59.29	53.30
	Avg	78.96	65.10	52.13	50.90
Post-Etching	M1	1320.80	1266.10	950.50	687.20
	M2	932.99	859.49	661.19	612.71
	M3	1289.80	1111.00	833.16	682.24
	M4	1298.70	1215.80	862.48	980.28
	M5	1484.90	959.18	902.87	1111.50
	Avg	1265.44	1082.31	842.04	814.79
Average Percent Change		1502.61	1502.61	1562.66	1515.32
Average Delta Ra (nm)		1186.48	1186.48	1017.22	789.91

Table C3. Trial 2 12 min HA Ra Measurements (nm)

		KE	KC	BE	BC
Pre-Etching	M1	231.77	178.92	201.27	206.76
	M2	197.68	178.60	193.97	197.47
	M3	209.92	181.44	208.72	197.25
	M4	231.60	183.54	211.37	179.81
	M5	256.10	189.21	212.80	187.30
	Avg	225.41	182.34	205.63	193.72
Post-Etching	M1	389.00	460.73	461.20	428.31
	M2	447.24	452.86	484.99	442.99
	M3	484.27	483.98	373.84	447.56
	M4	501.43	472.43	482.07	472.43
	M5	525.41	469.24	425.89	534.74
	Avg	469.47	467.85	445.60	465.21
Average Percent Change		108.27	156.58	116.70	140.15
Average Delta Ra (nm)		244.06	285.51	239.97	271.49

Table C4. Trial 2 20 min HA Ra Measurements (nm)

		KE	KC	BE	BC
Pre-Etching	M1	100.68	149.75	102.15	116.16
	M2	126.89	121.00	96.79	183.21
	M3	130.02	144.62	171.59	117.91
	M4	179.83	99.47	111.48	93.70
	M5	100.57	139.59	102.31	120.74
	Avg	127.60	130.88	116.86	126.35
Post-Etching	M1	1109.70	708.30	857.40	1033.40
	M2	1037.50	906.58	850.61	855.04
	M3	1117.90	936.27	894.55	1053.20
	M4	1131.30	1045.40	1167.40	1157.50
	M5	811.76	1402.60	1005.50	849.09
	Avg	1041.63	999.83	955.09	989.65
Average Percent Change		716.33	663.90	717.26	683.29
Average Delta Ra (nm)		914.03	868.95	838.23	863.30

Table C5. Trial 1 5 min HA + US Ra Measurements (nm)

		KE	KC	BE	BC
Pre-Etching	M1	109.30	99.70	49.20	54.20
	M2	105.80	76.92	59.98	55.08
	M3	135.24	79.40	58.81	46.83
	M4	138.35	78.60	46.58	39.37
	M5	138.60	102.55	41.15	43.49
	Avg	125.46	87.43	51.14	47.80
Post-Etching	M1	106.98	90.49	72.70	72.80
	M2	105.59	76.65	60.31	53.91
	M3	113.11	83.32	62.65	55.58
	M4	132.65	92.51	66.34	65.24
	M5	194.01	121.41	68.85	74.89
	Avg	130.47	92.87	66.17	64.49
Average Percent Change		4.00	6.22	29.38	34.92
Average Delta Ra (nm)		5.01	5.44	15.03	16.69

Table C6. Trial 1 12 min HA + US Ra Measurements (nm)

		KE	KC	BE	BC
Pre-Etching	M1	109.90	69.60	65.25	52.40
	M2	86.52	77.17	61.31	74.85
	M3	76.19	73.14	61.49	54.93
	M4	93.83	58.49	62.11	69.26
	M5	110.45	69.85	62.85	61.55
	Avg	95.38	69.65	62.60	62.60
Post-Etching	M1	950.90	837.50	686.30	549.96
	M2	601.60	795.86	660.49	509.63
	M3	889.73	636.23	699.15	608.73
	M4	1152.20	679.91	648.17	757.95
	M5	1366.60	695.87	625.88	854.98
	Avg	992.21	729.07	664.00	656.25
Average Percent Change		940.30	946.79	960.68	948.35
Average Delta Ra (nm)		896.83	659.43	601.40	593.65

Table C7. Trial 1 20 min HA + US Ra Measurements (nm)

		KE	KC	BE	BC
Pre-Etching	M1	139.50	197.50	106.40	115.10
	M2	82.65	89.44	116.21	105.07
	M3	113.11	88.59	110.97	81.34
	M4	84.06	90.64	120.87	109.49
	M5	94.38	94.39	98.51	94.33
	Avg	102.74	112.11	110.59	101.06
Post-Etching	M1	1044.30	1384.30	1333.50	1394.00
	M2	1317.90	1277.80	1215.50	1277.80
	M3	1394.90	1383.20	1263.70	1024.50
	M4	1428.10	1449.80	1610.70	1186.10
	M5	1752.50	2092.20	2025.30	1866.60
	Avg	1387.54	1517.46	1489.74	1349.80
Average Percent Change		1250.55	1253.53	1247.06	1235.59
Average Delta Ra (nm)		1284.80	1405.35	1379.15	1248.74

Table C8. Trial 2 5 min HA + US Ra Measurements (nm)

		KE	KC	BE	BC
Pre-Etching	M1	82.00	63.03	62.30	52.42
	M2	48.56	77.54	42.13	61.91
	M3	62.41	87.39	54.23	69.06
	M4	67.41	89.13	58.95	72.36
	M5	86.37	94.90	84.56	81.64
	Avg	69.35	82.40	60.43	67.48
Post-Etching	M1	70.20	59.30	47.30	55.17
	M2	54.50	59.60	60.34	50.88
	M3	66.15	65.85	61.66	61.36
	M4	81.35	106.68	62.86	74.27
	M5	81.67	127.24	68.46	107.24
	Avg	70.78	83.73	70.85	69.78
Average Percent Change		2.05	1.62	17.23	3.42
Average Delta Ra (nm)		1.42	1.33	10.41	2.31

Table C9. Trial 2 12 min HA + US Ra Measurements (nm)

		KE	KC	BE	BC
Pre-Etching	M1	68.42	52.90	54.06	59.20
	M2	71.84	59.30	51.17	48.36
	M3	58.73	59.57	51.51	49.86
	M4	49.46	62.39	55.21	56.00
	M5	45.45	60.34	47.34	63.06
	Avg	58.78	58.90	51.86	55.30
Post-Etching	M1	170.73	169.58	117.15	152.03
	M2	168.40	137.13	140.99	174.78
	M3	149.94	142.35	123.47	167.87
	M4	178.61	144.77	117.56	108.57
	M5	170.68	163.15	114.35	185.39
	Avg	167.67	151.40	122.70	157.73
Average Percent Change		185.26	157.04	136.62	185.24
Average Delta Ra (nm)		108.89	92.50	70.85	102.43

Table C10. Trial 2 20 min HA + US Ra Measurements (nm)

		KE	KC	BE	BC
Pre-Etching	M1	158.74	166.10	156.77	141.16
	M2	149.79	151.84	160.62	158.78
	M3	151.69	157.84	157.80	137.13
	M4	161.90	158.01	146.76	160.60
	M5	157.43	146.02	157.96	152.01
	Avg	155.91	155.96	155.98	149.94
Post-Etching	M1	1122.10	1104.10	1492.90	1187.70
	M2	1337.70	1112.10	991.79	1069.50
	M3	1164.90	995.19	1113.20	1232.30
	M4	1018.60	1385.10	996.73	1098.90
	M5	1121.80	1126.10	1272.40	1370.30
	Avg	1153.02	1144.52	1173.40	1191.74
Average Percent Change		639.55	633.84	652.27	694.83
Average Delta Ra (nm)		997.11	988.56	1017.42	1041.80

Table C11. Trial 1 12 min HA Sa Measurements (nm)

	K edge	K Center	B Edge	B Center
Pre-Etching	104.31	89.39	100.38	95.33
Post-Etching	132.04	99.89	147.35	139.06
Percent Change	26.59	11.76	46.79	45.87
Delta Sa (nm)	27.73	10.51	46.97	43.73

Table C12. Trial 1 20 min HA Sa Measurements (nm)

	K edge	K Center	B Edge	B Center
Pre-Etching	114.86	112.64	105.19	116.70
Post-Etching	1203.20	1252.50	1140.20	1231.60
Percent Change	947.57	1011.98	983.92	955.32
Delta Sa (nm)	1088.34	1139.86	1035.01	1114.90

Table C13. Trial 2 12 min HA Sa Measurements (nm)

	K edge	K Center	B Edge	B Center
Pre-Etching	104.31	89.39	100.38	95.33
Post-Etching	132.04	99.89	147.35	139.06
Percent Change	26.59	11.76	46.79	45.87
Delta Sa (nm)	27.73	10.51	46.97	43.73

Table C14. Trial 2 20 min HA Sa Measurements (nm)

	K edge	K Center	B Edge	B Center
Pre-Etching	114.86	112.64	105.19	116.70
Post-Etching	1203.20	1252.50	1140.20	1231.60
Percent Change	947.57	1011.98	983.92	955.32
Delta Sa (nm)	1088.34	1139.86	1035.01	1114.90

Table C15. Trial 1 5 min HA + US Sa Measurements (nm)

	K edge	K Center	B Edge	B Center
Pre-Etching	104.31	89.39	100.38	95.33
Post-Etching	132.04	99.89	147.35	139.06
Percent Change	26.59	11.76	46.79	45.87
Delta Sa (nm)	27.73	10.51	46.97	43.73

Table C16. Trial 1 12 min HA + US Sa Measurements (nm)

	K edge	K Center	B Edge	B Center
Pre-Etching	104.31	89.39	100.38	95.33
Post-Etching	132.04	99.89	147.35	139.06
Percent Change	26.59	11.76	46.79	45.87
Delta Sa (nm)	27.73	10.51	46.97	43.73

Table C17. Trial 1 20 min HA + US Sa Measurements (nm)

	K edge	K Center	B Edge	B Center
Pre-Etching	114.86	112.64	105.19	116.70
Post-Etching	1203.20	1252.50	1140.20	1231.60
Percent Change	947.57	1011.98	983.92	955.32
Delta Sa (nm)	1088.34	1139.86	1035.01	1114.90

Table C18. Trial 2 5 min HA + US Sa Measurements (nm)

	K edge	K Center	B Edge	B Center
Pre-Etching	302.22	266.36	307.29	231.17
Post-Etching	311.94	283.67	331.55	245.69
Percent Change	3.22	6.50	7.90	6.28
Delta Sa (nm)	9.72	17.32	24.26	14.52

Table C19. Trial 2 12 min HA + US Sa Measurements (nm)

	K edge	K Center	B Edge	B Center
Pre-Etching	103.79	100.47	112.23	106.32
Post-Etching	295.40	231.43	322.74	306.77
Percent Change	184.60	130.34	187.57	188.54
Delta Sa (nm)	191.60	130.96	210.51	200.45

Table C20. Trial 1 20 min HA + US Sa Measurements (nm)

	K edge	K Center	B Edge	B Center
Pre-Etching	265.82	218.85	245.13	240.05
Post-Etching	1318.10	1008.10	1327.30	1289.40
Percent Change	395.87	360.63	441.48	437.14
Delta Sa (nm)	1052.28	789.25	1082.17	1049.35

APPENDIX D. IMAGE FOCUS STACKING

Helicon Focus 8 software was used to stack microscope images to layer different levels of focus in order to create a clearer image. Figure D1 shows an image captured on the Olympus STM6 microscope (A) before and (B) after focus stacking. The process of using Helicon Focus 8 is detailed in Table D1.

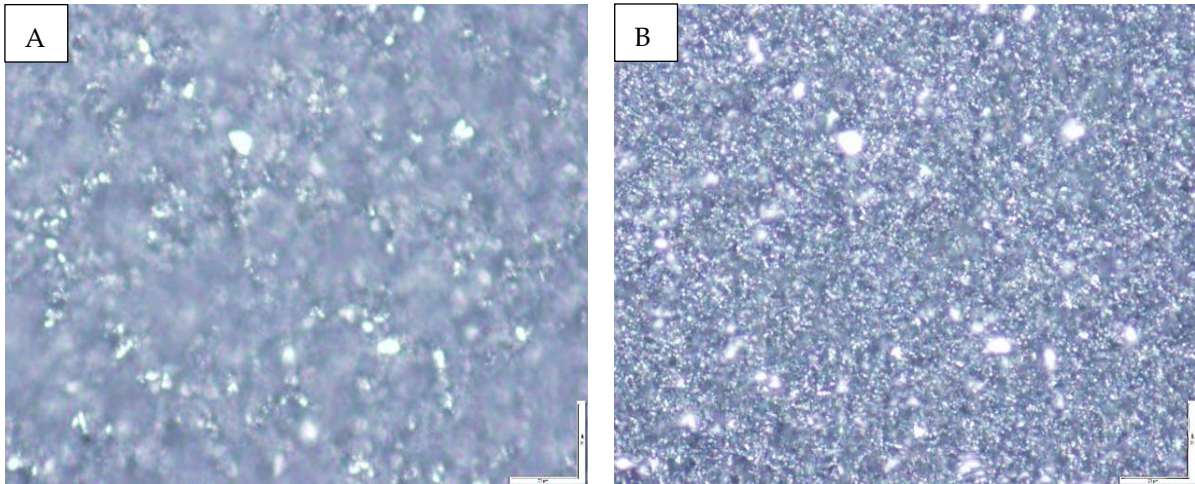
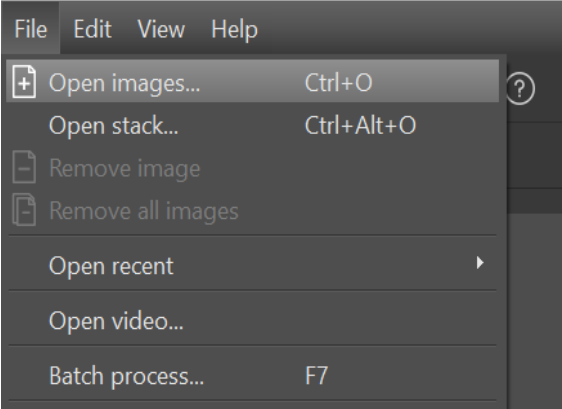
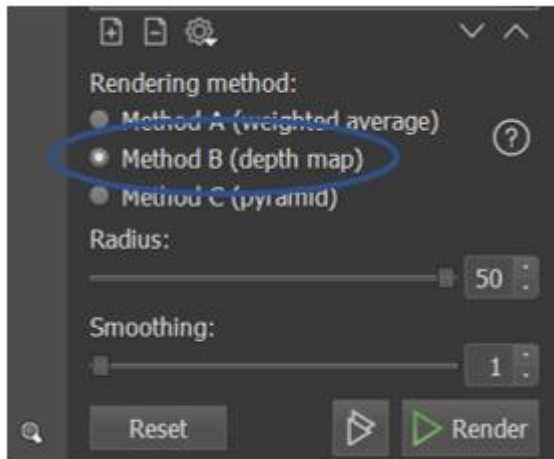
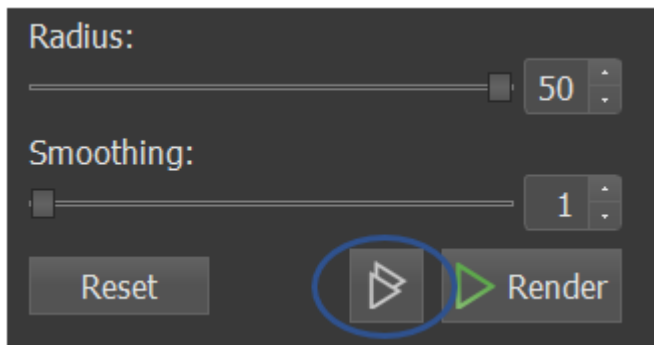


Figure D1. Microscope Images (A) Before and (B) After Focus Stacking

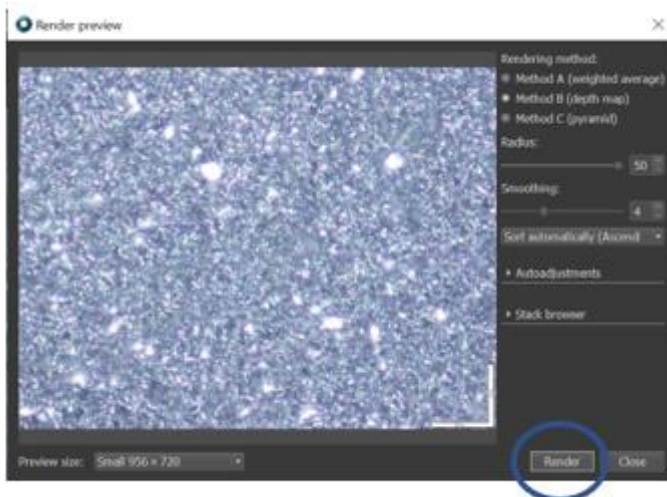
Table D1. Helicon Focus 8 Focus Stacking Process	
	<ol style="list-style-type: none">1. Upload the microscope images to be stacked. File → Open Images



2. Choose Render Method B (depth map).



3. Adjust the Radius and Smoothing settings as necessary to achieve better focus. Use the Render Preview Button to see real time adjustments.



4. Click the Render button to finalize the stacked image. Save the image. File → Save As

APPENDIX E. PUBLICATION

Craig M., Raval J., Tai B., Patterson A., and Hung W., “Effect of channel roughness on micro-droplet distribution in internal minimum quantity lubrication,” *Dynamics*, vol. 2, no. 4, pp. 336–355, 2022.